

Banner appropriate to article type will appear here in typeset article

Mesoscale Eddy-Induced Sharpening of Oceanic Tracer Fronts and its Parameterization

Yueyang Lu¹† and Igor Kamenkovich¹

¹Rosenstiel School of Marine, Atmospheric, and Earth Science, University of Miami, Miami, Florida

(Received xx; revised xx; accepted xx)

Oceanic fronts are ubiquitous and important features that form and evolve due to multiscale oceanic and atmospheric processes. For example, large-scale temperature and tracer fronts along the eastward extensions of the Gulf Stream and Kuroshio currents play key roles in the regional ocean environment and climate. The fronts cannot be realistically simulated by numerical models at spatial resolutions that do not resolve the oceanic mesoscale. This numerical study examines the relative importance of large-scale and mesoscale currents (“eddies”) in the front formation and evolution. Using an idealized model of the double-gyre system on both eddy-resolving and coarse-resolution grids, we demonstrate that the effect of eddies is to sharpen the large-scale front, whereas the large-scale current counteracts this effect. The eddy-driven frontogenesis is further described in terms of a recently proposed framework of generalized eddy-induced advection, which represents all those eddy effects on tracers that are not due to eddy-induced mass fluxes and are traditionally parameterized by isopycnal diffusion. In this study the generalized advection is represented using an effective eddy-induced velocity (EEIV), which is the speed at which eddies move tracer contours. The advantage of this formulation is that the frontal sharpening can be readily reproduced by EEIVs, whereas it cannot be modeled as a diffusive process. A proposed closure (“parameterization”) for EEIV based on large-scale properties shows promise in representing frontogenesis in coarse-resolution simulation. This study demonstrates advantages of using an advective rather than diffusive framework for representing eddy effects in coarse-resolution models.

Key words:

1. Introduction

Fronts, characterized by narrow bands of enhanced gradients of physical and biogeochemical tracers such as temperature, dissolved carbon and nutrients, are ubiquitous in the upper ocean. The width of ocean fronts can range from a few meters to tens of kilometers (McWilliams 2021), and processes at various spatial scales play a role in front formation and evolution (Belkin *et al.* 2009). Fronts can facilitate the transfer of the tracers from the surface to the ocean interior and play an important role in the climate and ocean ecological systems

† Email address for correspondence: yueyang.lu@miami.edu

(D'Asaro *et al.* 2011; Ferrari 2011; Lohmann & Belkin 2014). The fronts associated with strong large-scale currents, such as western boundary current extensions and the Antarctic Circumpolar Current, can have length extending for hundreds of kilometers and are of particular importance. These large-scale fronts can act as dynamical barriers to cross-frontal transport and mixing (Rypina *et al.* 2011, 2013) and impact the lower troposphere and mid-latitude climate (Small *et al.* 2008; Minobe *et al.* 2008; Seo 2023). The goal of this study is to examine the role of ocean mesoscale eddies [length scale of $O(10\text{--}100)$ km; “eddies” hereafter] in the evolution of large-scale temperature and tracer fronts associated with the eastward extensions of western boundary currents.

Oceanic mesoscale eddies pervade the vicinity of large-scale currents and can influence the fronts in several important ways. Baroclinic instability of these currents, which is one of the main mechanisms for eddy generation, can be expected to weaken the vertical shear and density fronts (Pedlosky 1987; Vallis 2017). On the other hand, eddies can have a straining effects that generate and sharpen the associated fronts (e.g., Berloff 2005; Waterman & Jayne 2011). Oceanic components in modern climate models, however, do not fully resolve mesoscale eddies (Meijers 2014; Hewitt 2020), which leads to biases in the simulated ocean state. For example, non-eddy-resolving models simulate much weaker sea surface temperature (SST) fronts in the Gulf Stream extension than is seen in eddy-resolving ocean models or observations (Kirtman 2012; Parfitt *et al.* 2016; Siqueira & Kirtman 2016). The biases in the SST front in these simulations can impact the atmospheric temperature front (Parfitt *et al.* 2016), storm tracks (Small *et al.* 2014), and climate variability (Kirtman 2012).

Mesoscale eddies can affect tracer fronts through multiple processes: the dynamic feedback of eddies on the large-scale current, the eddy-induced mass fluxes, and the eddy stirring and mixing. Most of previous studies have focused on understanding and parameterization of the first two processes. The dynamic effect of eddies refers to the eddy stirring of momentum (Waterman *et al.* 2011) and potential vorticity (PV; Berloff 2005; Waterman & Jayne 2011; Mana & Zanna 2014; Bachman *et al.* 2017; Ryzhov & Berloff 2022), which acts as both dissipation and a driving force for the large-scale current, which in turn advects the tracers and influences the fronts. Shevchenko & Berloff (2015) discussed this dynamic eddy effect on the PV front and found weaker fronts along the eastward jet extension in a quasi-geostrophic model at lower horizontal resolutions. The second effect, eddy-induced mass transport, is equivalent to an eddy-induced tracer advection and is commonly parameterized by the Gent–McWilliams framework (e.g. Gent & McWilliams 1990; Gent *et al.* 1995) that flattens isopycnals. This effect has been extensively studied and recent efforts mostly focus on advancing the GM parameterization (e.g. Grooms 2016; Grooms & Kleiber 2019; Bachman 2019; Bachman *et al.* 2020).

This study focuses on the third process, which is the most direct effect of eddies on tracers. It is traditionally treated as isotropic eddy-induced diffusion (Redi 1982). However, several recent studies have revealed the importance of its anisotropic diffusive (Bachman *et al.* 2015, 2020; Kamenkovich *et al.* 2021; Haigh *et al.* 2021a; Zhang & Wolfe 2022; Kamenkovich & Garraffo 2022) and advective (Haigh *et al.* 2021b; Lu *et al.* 2022) properties for tracer distributions. Most importantly, several studies of eddy diffusion demonstrate persistent up-gradient (negative) diffusion, which implies a mechanism of tracer filamentation and frontal sharpening (“frontogenesis”). Practical implementation of the up-gradient diffusion, however, leads to numerical instability, and negative diffusion conflicts with the analogy between turbulent and molecular diffusive mixing. The eddy-induced advection, in contrast, can be an appropriate model for the large-scale frontal development because the frontogenesis is essentially an advective process (McWilliams 2021). In addition, the transport barriers associated with the fronts are assumed to result from the joint action of the large-scale and eddy advections (Berloff *et al.* 2009; Kamenkovich *et al.* 2019). The advective formulation has

Parameter	Value	Description
$L_x \times L_y$	$3840 \times 3840 \text{ km}$	Horizontal domain dimensions
$\Delta x, \Delta y$	3.75 km	Horizontal grid spacing
H_1, H_2, H_3	(0.3, 0.7, 3) km	Initial isopycnal layer thicknesses
f_0	$4.4 \times 10^{-5} \text{ s}^{-1}$	Coriolis parameter at the southern boundary
β	$2 \times 10^{-11} \text{ m}^{-1} \text{ s}^{-1}$	Meridional gradient of Coriolis parameter
ρ_0	1035 kg m^{-3}	Reference density
ν	$100 \text{ m}^2 \text{ s}^{-1}$	Laplacian horizontal viscosity
g	9.8 m s^{-2}	Gravity
g'	(0.01, 0.0003) m s^{-2}	Reduced gravities at the upper interface of layer $k = 2, 3$
C_d	0.003	Linear bottom drag coefficient
$ \mathbf{u}_* $	0.1 m s^{-1}	Near-bottom velocity magnitude
τ_0	0.22 N m^{-2}	Wind stress amplitude
r	$2 \times 10^{-8} \text{ s}^{-1}$	Relaxation rate for the upper layer thickness
κ_{tr}	$100 \text{ m}^2 \text{ s}^{-1}$	Background isopycnal tracer diffusivity

Table 1: List of parameters used in the high-resolution model.

84 a clear advantage over the diffusive framework in this regard. For example, a perfect barrier
 85 naturally results from the full cancellation between the large-scale and eddy-induced velocity
 86 (zero “residual velocity”), while the barrier cannot be guaranteed for an arbitrary tracer if the
 87 effects of eddies are diffusive. Recently, Lu *et al.* (2022) has proposed a generalized eddy-
 88 induced advection to quantify the direct eddy effects, and used it to successfully reproduce
 89 the eddy-induced stirring and dispersion in a high-resolution model. This study will further
 90 advance this approach, and will examine the extent to which the stirring effects of eddies on
 91 a large-scale front can be modeled by eddy-induced advection and be parameterized in terms
 92 of large-scale quantities.

93 The paper is organized as follows. Section 2 describes the ocean models used in this
 94 study. Section 3 derives the tracer eddy forcing that includes the effects of eddies on a
 95 large-scale front, the frontogenesis equation and the generalized advective model of the eddy
 96 forcing. Section 4 examines the eddy effects on the front via the sensitivity experiments and
 97 analysis of the equation. Section 5 discusses performance of the tracer simulations with the
 98 eddy-induced advection. Section 6 offers conclusions.

99 2. Model

100 2.1. Primitive equation ocean model

101 We use the Modular Ocean Model version 6 (MOM6, Adcroft 2019) to solve the adiabatic
 102 shallow-water equations in a square basin with flat bottom. The model represents a wind-
 103 driven mid-latitude, double-gyre ocean circulation in the Northern Hemisphere, whose setup
 104 is motivated by Cooper & Zanna (2015). The model has three stacked isopycnal layers with
 105 a free surface. Key parameters are summarized in table 1.

The momentum and continuity equations in layer k ($k = 1, 2, 3$ with $k = 1$ denoting upper

layer) are

$$\frac{\partial \mathbf{u}_k}{\partial t} + \frac{f + \zeta_k}{h_k} \hat{z} \times (\mathbf{u}_k h_k) + \nabla \left(M_k + \frac{|\mathbf{u}_k|^2}{2} \right) = \delta_{1k} \frac{\tau}{\rho_0 h_1} - \delta_{3k} \frac{C_d}{h_k} |\mathbf{u}_*| \mathbf{u}_k + \nabla \cdot \boldsymbol{\sigma}_k, \quad (2.1a)$$

$$\frac{\partial h_k}{\partial t} + \nabla \cdot (\mathbf{u}_k h_k) = R_h(h_k). \quad (2.1b)$$

where \mathbf{u}_k is the horizontal velocity, $f = f_0 + \beta y$ is the planetary vorticity following the beta-plane approximation, $\zeta_k = \hat{z} \cdot \nabla \times \mathbf{u}_k$ is the vertical component of relative vorticity, \hat{z} is the unit vector in the vertical direction, h_k is layer thickness, δ_{ij} is the Kronecker delta, ∇ is the horizontal (isopycnal) gradient, and M_k is the Montgomery potential. The wind stress τ is steady, asymmetric, and non-zonal (figure 1a). The bottom stress is calculated from a linear drag law that depends on a prescribed near-bottom flow speed $|\mathbf{u}_*|$ and coefficient C_d . The horizontal and vertical stress tensor $\boldsymbol{\sigma}_k$ is parameterized by a Laplacian viscosity. A relaxation term $R_h(h_k) = \delta_{1k} r (h_r - h_k)$ is applied to the upper layer thickness to keep it close to a reference profile h_r at a rate of r . The relaxation is needed to maintain a sharp eastward extension of the boundary current. Detailed description of the terms in the equations is in Appendix A.

The square domain ($L_x \times L_y = 3840 \text{ km} \times 3840 \text{ km}$) is closed by solid boundaries, where free slip and no normal flux boundary conditions are applied. The equations are discretized on a uniform high-resolution (eddy-resolving) grid of 3.75 km resolution (1024^2 grid cells) with a time step of 50 s. We also use a coarse-resolution (non-eddy-resolving) grid of 60 km resolution (64^2 grid cells).

The model is spun up for 20 years from the state of rest to reach a statistically steady flow. It is then run for 4 additional years with all model fields saved every 6 hours as both the 6-hour averaged quantities and snapshots. Figures 1b-d show the ocean circulation in the eddy-resolving simulation. The model develops a strongly eddying double-gyre flow, separated by a meandering jet extending from the western boundary and representing the Gulf Stream or Kuroshio extension. It will be referred to as the Eastward Jet Extension (EJE) hereafter. A near-zonal front of potential vorticity (PV), characterized by large meridional PV gradients, is formed along the EJE (figure 1c).

2.2. Tracer model

The evolution of tracer concentration c in each layer is governed by

$$\frac{\partial (hc)}{\partial t} + \nabla \cdot (\mathbf{U}c) = \nabla \cdot (\kappa_{tr} h \nabla c) + R_{tr}(c) \quad (2.2)$$

where $\mathbf{U} = \mathbf{u}h$ is the horizontal mass flux, $R_{tr}(c) = r_{tr}h(c_r - c)$ is relaxation of the tracer back to its initial distribution c_r , r_{tr} is the relaxation rate, and the layer subscript is omitted hereafter. The relaxation is applied in the upper layer only and is intended to mimic interactions with the atmosphere and prevent the tracer field from rapid homogenization. We set the subgrid tracer diffusivity $\kappa_{tr} = 100 \text{ m}^2 \text{ s}^{-1}$ for all tracer simulations in this study. Tracers are initialized on the first day of year 21 and are simulated for 2 years.

We consider two idealized tracers with spatial distributions relevant to the real ocean properties. The tracers are initialized with a vertically and zonally uniform distribution. For the robustness of the conclusions, we chose tracers with very different initial meridional profiles. One tracer has an initial southward gradient (values increasing from north to south) generally consistent with the observed annual-mean sea surface temperature (SST), and a

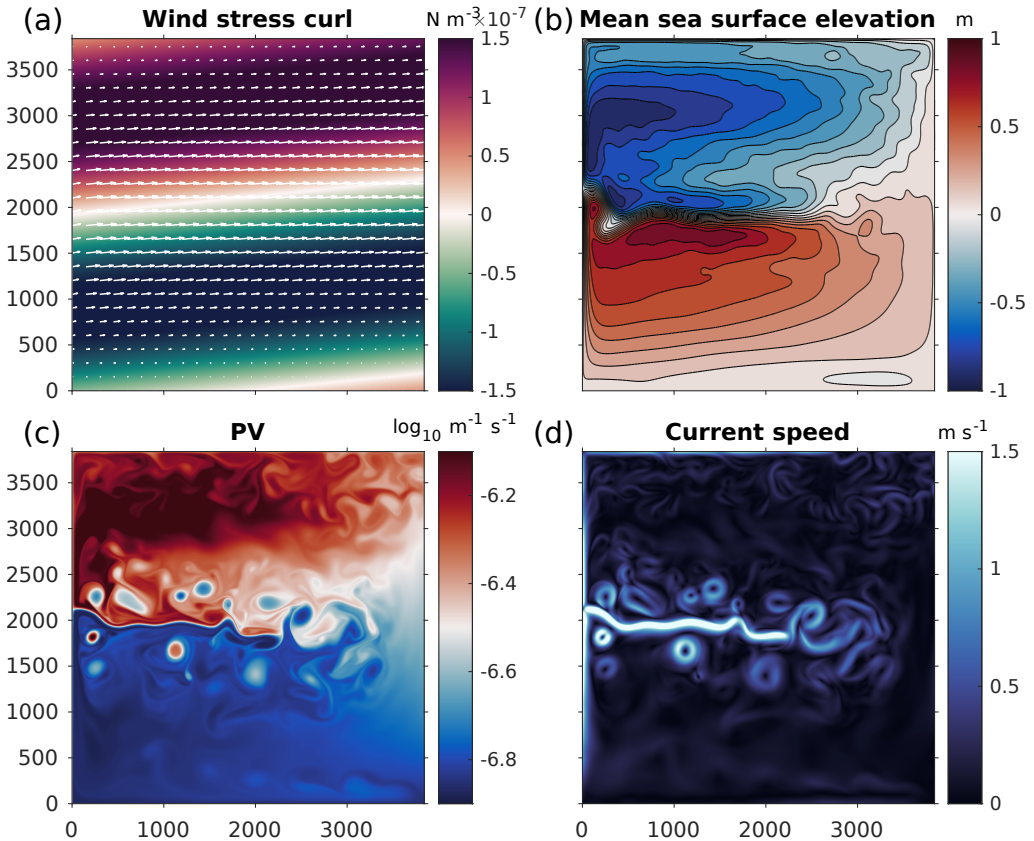


Figure 1: High-resolution simulations. (a) Wind stress vector and its curl. (b) Sea surface elevation averaged from year 21 to year 23. Snapshots of (c) potential vorticity and (d) current speed at day 120 year 21. All fields are shown in the upper layer.

144 relaxation time scale of $1/r_{tr} = 400$ d that mimics the dependence of the surface heat flux on
 145 SST (Haney 1971). We call it a “passive temperature” tracer. The other tracer has an initial
 146 northward gradient (values increasing south to north) that is typical of chemical tracers with
 147 higher solubility at cold temperatures such as CFC-11. It has a relaxation time scale of 125
 148 d that mimics the time scale associated with the gas transfer of CFC-11 with the atmosphere
 149 (England *et al.* 1994). We call it a “chemical” tracer. Despite having initial profiles analogous
 150 to SST and CFC-11, these idealized tracers should not be interpreted as realistic simulations
 151 of these real-ocean properties. For additional analysis of the sensitivity of the results to
 152 tracers, we will also use eight additional color-dye tracers with initial linear and sinusoidal
 153 distributions (Appendix B).

154 Figure 2 shows the initial profiles and subsequent solutions in the high-resolution model.
 155 For the passive temperature, the western boundary currents bring warm (cold) water from
 156 subtropical (subpolar) gyre to the latitude of the EJE ($y \approx 2000$ km), where the warm and
 157 cold currents meet and continue eastward. The warm and cold waters retain their temperature
 158 contrast avoiding strong mixing with each other, indicating a presence of a partial mixing
 159 barrier along the EJE axis (Rypina *et al.* 2011, 2013; Kamenkovich *et al.* 2019). This
 160 confluence of cold and warm water creates a large negative meridional gradient (i.e. a sharp
 161 temperature front) along the jet extension. Similar features are observed for the chemical
 162 tracer, except that the front is characterized by large positive meridional gradient.

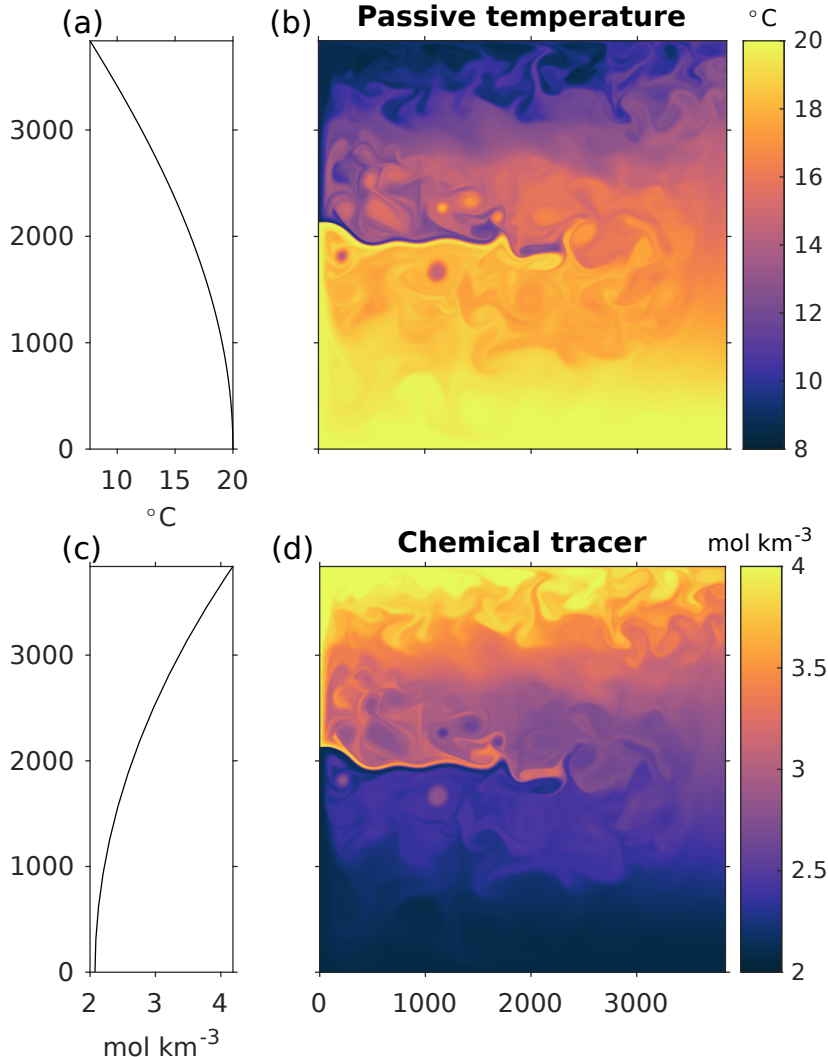


Figure 2: (a) Initial meridional profile and (b) upper layer tracer solution at day 120 year 21 for the passive temperature tracer. (c)-(d) Same but for the chemical tracer.

163 The focus of this study is on the effect of mesoscale eddies on a large-scale tracer front.
 164 For this purpose, we also perform tracer simulations on a coarse-resolution grid in which the
 165 eddies are not resolved:

$$166 \quad \frac{\partial(h_L c_L)}{\partial t} + \nabla_c \cdot (\mathbf{U}_L c_L) = \nabla_c \cdot (\kappa_{tr} h_L \nabla c_L) + R_{tr}(c_L) + \mathcal{D} \quad (2.3)$$

167 where the subscript L denotes the large-scale fields on the coarse grid, ∇_c is a horizontal
 168 gradient on the coarse grid, and \mathcal{D} is a term representing subgrid eddy effects.

169 Eddies can affect large-scale tracer concentration c_L through three pathways: (i) the dy-
 170 namical modulation of the large-scale velocity \mathbf{u} in (2.1a); (ii) the eddy-induced mass/density
 171 transport $\mathbf{U}_L - \mathbf{u} h_L$ and its effects on h_L in (2.1b) and c_L in (2.3); and (iii) the direct eddy
 172 tracer effect \mathcal{D} to be discussed below. The coarse-grid solution c_L will be different from the
 173 fine-grid solution c from (2.2) unless all three effects are represented accurately.

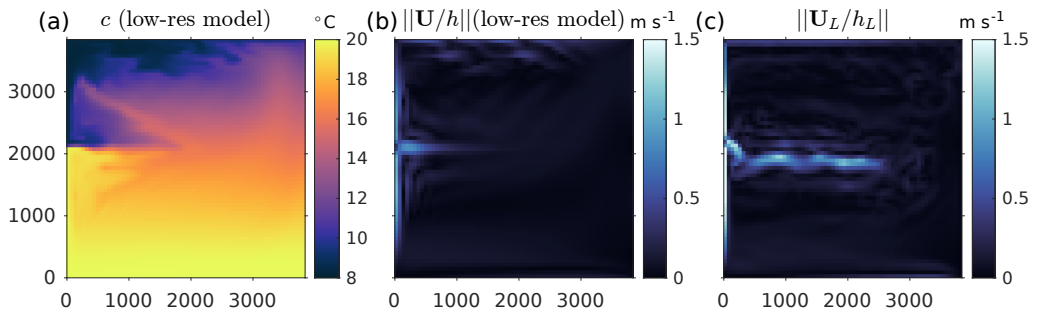


Figure 3: (a) The passive temperature tracer and (b) residual velocity speed (large scale plus GM velocities) simulated in the non-eddy-resolving model. (c) The residual velocity speed derived from the eddy-resolving model solution. Its derivation is given in section 3.1. All fields are diagnosed at day 120 year 21 in the upper layer. Note that in this study we mainly use (c).

174 Full coarse-grid simulations, that is, solutions of (2.1) and (2.2) on the coarse grid,
 175 predictably result in large biases in the position and intensity of the EJE and the associated
 176 tracer front. The biases manifest the importance of the dynamic and density effects of eddies
 177 (i)-(ii) that are missing in the coarse-grid simulations. Although these biases can potentially
 178 be alleviated by parameterizations of the momentum fluxes in (2.1a) and eddy-induced mass
 179 fluxes in (2.1b), e.g., by using the momentum eddy viscosity and the Gent-McWilliams
 180 (GM) closure (Gent *et al.* 1995), respectively, our attempt to use constant coefficients in both
 181 schemes failed to improve simulation of the front. Figures 3a-b show the passive temperature
 182 tracer and the residual velocity: the sum of the large-scale velocity solved by the model and
 183 the eddy-induced velocity parameterized by the GM scheme, in the coarse-grid simulation.
 184 A typical GM coefficient of $400 \text{ m}^2 \text{ s}^{-1}$ and a scale-selective Smagorinsky eddy viscosity
 185 (Smagorinsky 1963) with a nondimensional parameter of 0.15 are used. We see that the
 186 tracer front barely extends eastward and has a different position from the high-resolution
 187 front (figure 2b), which is mainly a result of a biased EJE (figure 3b).

188 In this study, we chose to focus on the direct stirring effect of eddies (term \mathcal{D}) and to
 189 derive \mathbf{U}_L directly from the eddy-resolving solution instead of solving it in the non-eddy-
 190 resolving model. This approach ensures that the tracer on the coarse grid is advected by
 191 the “correct” residual flow \mathbf{U}_L , and we will demonstrate that it is not enough to represent
 192 a realistic tracer front. We employ the offline method that uses precalculated mass flux and
 193 layer thicknesses to solve the tracer equation (2.3). The method has been used for studies
 194 on the importance of mesoscale currents in tracer transports (Kamenkovich *et al.* 2017,
 195 2021; Kamenkovich & Garraffo 2022) and the representation of eddy-induced advection and
 196 diffusion (Lu *et al.* 2022). Note that by using such an exact full mass flux, we do not need
 197 to include the GM closure, and our study is concerned with those eddy effects that even a
 198 “perfect” parameterization of the eddy mass fluxes cannot represent.

199 To ensure that there are no spurious sources of tracer mass, the large-scale layer thickness
 200 used in (2.3) is solved from the continuity on the coarse grid, with prescribed large-scale
 201 mass fluxes:

$$202 \quad \frac{\partial h_L}{\partial t} + \nabla_c \cdot \mathbf{U}_L = R_h(h_L), \quad (2.4)$$

203 where the relaxation rate of layer thickness has the same value as the high-resolution model.
 204 The continuity and tracer time steps on coarse grid are 600 s.

205 We estimate the errors due to the offline calculations of tracer flux divergence, by comparing
 206 online and offline simulations of the passive temperature tracer. We confirmed that the errors

207 are sufficiently small to warrant the use of the offline method for passive tracer simulations.
 208 The comparison is described in Appendix C.

209 **3. Tracer eddy forcing and frontogenesis equation**

210 In this section, we discuss a definition of the eddy forcing, derive the equation for the
 211 meridional tracer gradient that governs the evolution of the EJE front, and briefly discuss the
 212 generalized advective model for eddy effects on the tracer front.

213 *3.1. Tracer eddy forcing*

214 Mesoscale eddies lead to cross-scale transfer of energy and tracer (and its variance), so a
 215 non-eddy-resolving tracer model needs a subgrid tracer “forcing” to account for contributions
 216 of the unresolved scales to the large (resolved) scales. We define this tracer eddy forcing as
 217 the source term that augments the coarse-grid tracer solution towards a reference “truth”,
 218 given a particular large-scale flow on the coarse grid (Berloff *et al.* 2021; Agarwal *et al.*
 219 2021). In this study, we define the truth as the coarse-grained eddy-resolving tracer solution.
 220 Here, the coarse graining of a fine-grid solution is defined as spatial averaging over the
 221 coarse-grid cell of 60 by 60 km (16 by 16 fine grid points). The corresponding eddy forcing
 222 is obtained by coarse-graining the high-resolution tracer equation (2.2), subtracting the result
 223 from the coarse-grid equation (2.3), and requiring that $c_L = \langle c \rangle$ where angle bracket is the
 224 coarse-graining operator, which gives

$$225 \quad \frac{\partial(h_L\langle c \rangle)}{\partial t} + \nabla_c \cdot (\mathbf{U}_L\langle c \rangle) = \nabla_c \cdot (\kappa_{tr} h_L \nabla \langle c \rangle) + R_{tr}(\langle c \rangle) + \mathcal{D}_e \quad (3.1)$$

226 Here, \mathcal{D}_e is the tracer eddy forcing that can be diagnosed from the high-resolution model
 227 solutions, the given large-scale flow \mathbf{U}_L and layer thickness h_L , and the coarse-grained tracer
 228 $\langle c \rangle$:

$$229 \quad \mathcal{D}_e = \frac{\partial(h_L\langle c \rangle)}{\partial t} - \frac{\partial\langle hc \rangle}{\partial t} + \nabla_c \cdot (\mathbf{U}_L\langle c \rangle) - \langle \nabla \cdot (\mathbf{U}c) \rangle \\ 230 \quad + \langle \nabla \cdot (\kappa_{tr} h \nabla c) \rangle - \nabla_c \cdot (\kappa_{tr} h_L \nabla \langle c \rangle) + \langle R_{tr}(c) \rangle - R_{tr}(\langle c \rangle). \quad (3.2)$$

231 At this point, the entire coarse-resolution system (eqs. 2.4, 3.1, and 3.2) hinges on the
 232 definition of the large-scale mass flux \mathbf{U}_L , which needs to be prescribed. We choose to define
 233 it as a coarse-grained and time-filtered high-resolution mass flux:

$$234 \quad \mathbf{U}_L = \langle \bar{\mathbf{U}} \rangle \quad (3.3)$$

235 where the overbar is a 180-day sliding average, which, together with the coarsening removes
 236 the mesoscale variability. This is motivated by the fact that mesoscale eddies are often
 237 characterized by time scales of a few months. We also tested a 2-year time mean, and
 238 confirmed that it does not change our main conclusions in this study. To make sure that the
 239 divergence of \mathbf{U} is preserved on the coarse grid, we decompose \mathbf{U} into its divergent and
 240 rotational components and then coarse grain them separately. The derived \mathbf{U}_L is shown in
 241 figure 3c. It retains the intensity and position of the EJE in the high-resolution model. Further
 242 details on its derivation are given in Appendix D.

243 The diagnosed eddy forcing \mathcal{D}_e has complex spatial structure (figure 4a-c). Its high-
 244 magnitude values are concentrated along the EJE, where eddies cause significant redistributions
 245 of a large-scale tracer. The standard deviation exceeds the time-mean in most of the
 246 domain, indicating significant time variability in the eddy effects.

247 According to (2.3), (3.1) and (3.2), \mathcal{D}_e should in theory be able to augment the coarse-grid

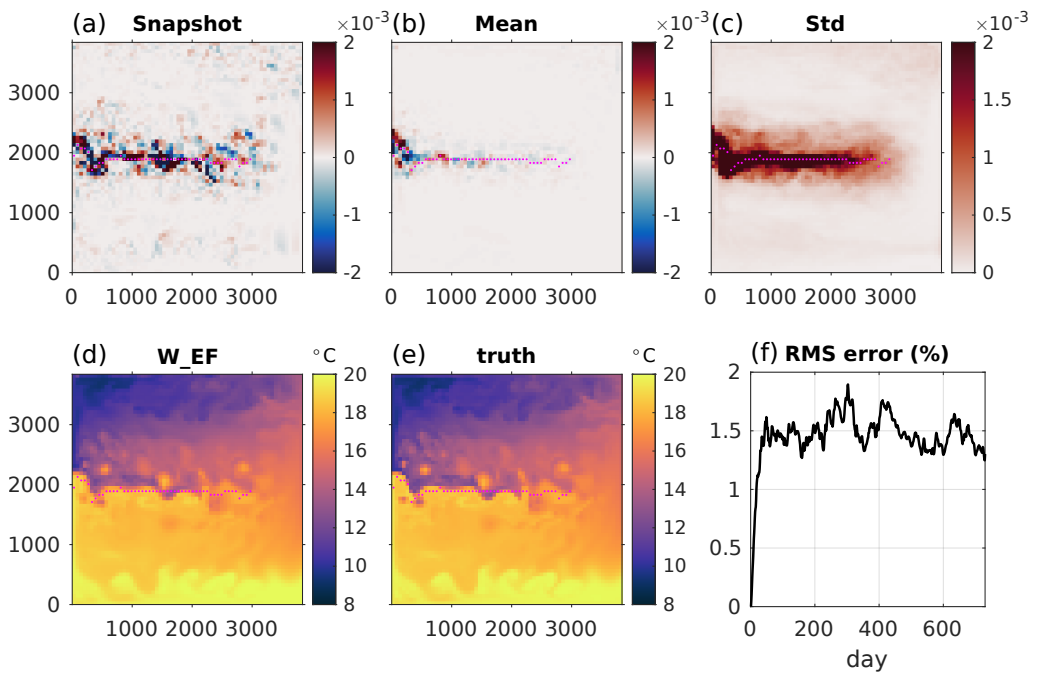


Figure 4: Eddy forcing for the passive temperature tracer and its skill of augmenting the coarse grained solution towards the truth. (a) Snapshot, (b) time-mean and (c) standard deviation over 2 years (years 21-22). Unit is [$^{\circ}\text{C m s}^{-1}$]. (d) The passive temperature solved in the W_EF simulation. (e) The coarse-grained high-resolution solution (“truth”). (f) RMS value (multiplied by 100) of the relative error in the tracer in W_EF (relative to the truth) vs. time. Y-axis units are [%]. Snapshots are in the upper layer on day 361 year 21. Magenta dots are the EJE core defined by the maximal speed of the large-scale velocity \mathbf{u}_L in the EJE region ($0 < x < 3000$ km, $1600 < y < 2400$ km).

model toward the true tracer concentration $\langle c \rangle$. To explore the extent to which it applies to our numerical application, we simulated the passive temperature tracer in a control experiment with $\mathcal{D} = \mathcal{D}_e$ (W_EF) in tracer equation (2.3). However, we found that after only about 10 days, the augmented solution significantly diverges from the truth. This is because \mathcal{D}_e has a complex spatial pattern and temporal variability, and its augmenting efficiency depends critically on its spatial and temporal relation to the large-scale flow. Even small errors in this relation can quickly grow leading to large local biases in the solution. A similar issue was reported by Berloff *et al.* (2021) in their PV eddy forcing. To alleviate this deficiency, we ran the W_EF experiment with additional relaxation of the solution toward the truth, saved the relaxation forcing, and added it to the original \mathcal{D}_e to get a new eddy forcing \mathcal{D}_e^\dagger . In this case, small differences due to the numerical errors are absorbed in \mathcal{D}_e^\dagger . The relaxation term is verified to be small compared to the original \mathcal{D}_e , but sufficient to suppress growing numerical errors. We confirmed that \mathcal{D}_e^\dagger is statistically nearly identical to \mathcal{D}_e , and deviations due to the added relaxation forcing have an area r.m.s. value of about 6% of \mathcal{D}_e . We reran W_EF with the new forcing \mathcal{D}_e^\dagger and no additional relaxation and confirmed that the solution indeed stays close to the truth with a relative difference of less than 2% (figure 4d-f). Henceforth, we will use the new eddy forcing for the following analysis, and we will omit superscript “ \dagger ”.

To demonstrate the importance of eddies in the large-scale tracer distribution, we run an experiment with $\mathcal{D} = 0$ (NO_EF). Figures 5a-b compare the passive temperature solutions in NO_EF and W_EF. The most important difference is in the vicinity of the front along

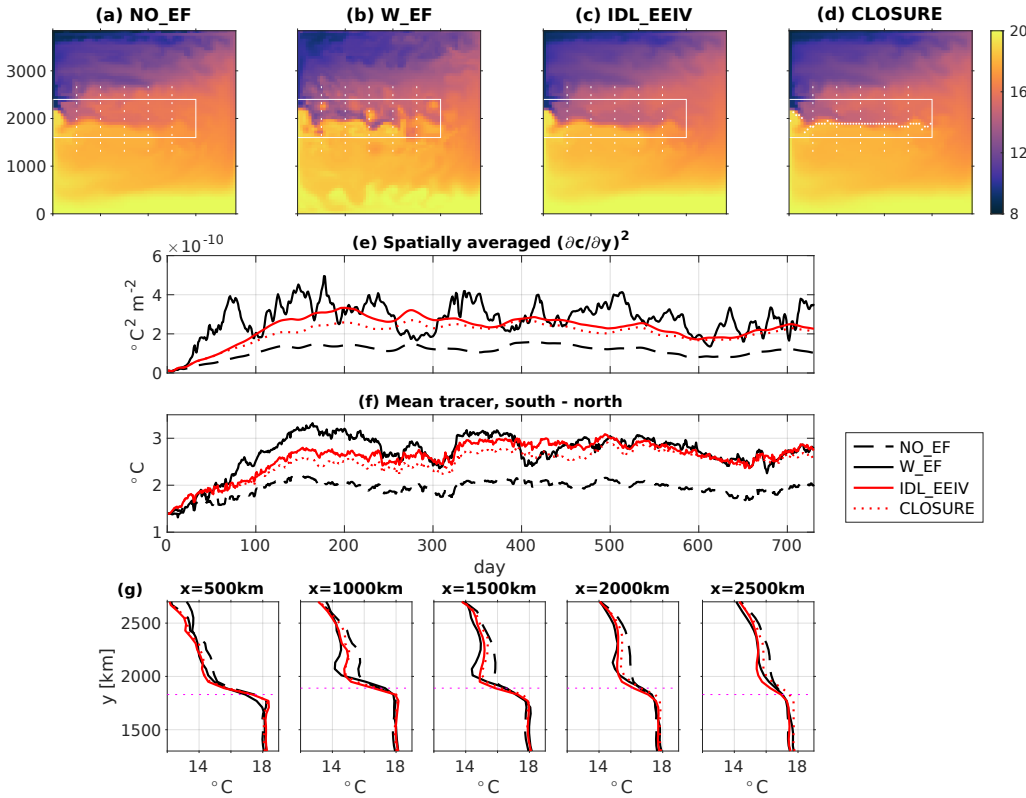


Figure 5: Passive temperature tracer solutions in the (a) NO_EF, (b) W_EF, (c) IDL_EEIV and (d) CLOSURE experiments on day 361 year 21. Unit is $^{\circ}\text{C}$. Solid white lines show the boundaries of the EJE region in which the spatial average is performed. Zonal dots are the EJE core that divides the EJE region into the “north-of-jet” and “south-of-jet” region. Meridional dotted lines show the longitudes at which the profiles are diagnosed. Data are in the upper layer. (e) The squared meridional tracer gradient averaged along the EJE core.

(f) The difference between the tracer inventory area-averaged in the south-of-jet and north-of-jet regions. (g) The meridional profiles of the 2-year (years 21-22) mean tracers in all the experiments.

268 the EJE. There is less warm (cold) water at the southern (northern) side of the EJE core in
 269 NO_EF, leading to a significantly weaker temperature front. We can quantify the strength of
 270 the front by three metrics: the squared meridional tracer gradient averaged along the EJE
 271 core (figure 5e), the tracer difference between the south and north of the EJE (figure 5f),
 272 and the meridional tracer profiles across the EJE (figure 5g). We see that the gradient on the
 273 EJE in W_EF is nearly twice as large as in NO_EF. The temperature difference in W_EF is
 274 about 1 degree (50%) larger than in NO_EF. The meridional profiles also show sharper tracer
 275 gradients in different positions of EJE in W_EF than NO_EF. These results demonstrate that
 276 the front is significantly weaker in the absence of eddy stirring, despite the correct large-scale
 277 advection \mathbf{U}_L and eddy mass fluxes. This conclusion suggests that the stirring by mesoscale
 278 eddies significantly sharpens the front, which will be further confirmed in the following
 279 sections.

3.2. Frontogenesis equation

281 To explore the eddy-driven sharpening of the EJE front (“frontogenesis”), we derive the
 282 equation governing the evolution of a tracer gradient on coarse grid. We first combine the
 283 coarse-grid tracer equation (2.3) and continuity (2.4) to get the advective form of the tracer
 284 equation:

$$\frac{\partial c_L}{\partial t} + \mathbf{u}_L \cdot \nabla_c c_L = \frac{\mathcal{D}}{h_L} + \frac{\nabla_c \cdot (\kappa_{tr} h_L \nabla_c c_L)}{h_L} + \frac{R_{tr}(c_L) - c_L R_h(h_L)}{h_L} \quad (3.4)$$

where $\mathbf{u}_L = U_L/\bar{h}_L$ is the large-scale (residual) velocity that includes the effect of eddy-induced mass flux. Due to the beta-effect, tracer gradients along the near-zonal EJE front are nearly meridional, and we focus our analysis on the meridional direction. Applying $[(\partial_y c_L)\partial_y]$ to (3.4), we arrive at the equation of the (squared) meridional tracer gradient (a.k.a. frontogenesis equation; Mudrick 1974; Hoskins 1982; McWilliams 2021):

$$\begin{aligned}
& \frac{\partial}{\partial t} (\partial_y c_L)^2 = L + E + A + R, \\
& L = -2(\partial_y c_L) \partial_y (\mathbf{u}_L \cdot \nabla_c c_L), \\
& E = 2(\partial_y c_L) \partial_y (\mathcal{D}/h_L), \\
& A = 2(\partial_y c_L) \partial_y (\nabla_c \cdot (\kappa_{tr} h_L \nabla_c c_L)/h_L), \\
& R = 2(\partial_y c_L) \partial_y ((R_{tr}(c_L) - c_L R_h(h_L))/h_L).
\end{aligned} \tag{3.5}$$

296 Here L describes the effects of the large-scale advection which consist of two distinct
 297 mechanisms: (i) the large-scale advection of the squared tracer gradient $L_{adv} = -\mathbf{u}_L \cdot$
 298 $\nabla_c (\partial_y c_L)^2$ and (ii) the confluence of large-scale velocity $L_{con} = -2(\partial_y c_L)(\partial_y \mathbf{u}_L \cdot \nabla_c c_L)$,
 299 where $\partial_y \mathbf{u}_L$ is the meridional velocity gradient tensor. E is the eddy effect on the tracer
 300 gradient, and A and R represent the effects of subgrid diffusion and relaxations, respectively.

3.3. The generalized advective-diffusive model

302 For an approximation $\hat{\mathcal{D}}_e$ of the full eddy forcing \mathcal{D}_e , we use here a generalized advective–diffusive framework recently proposed by Lu *et al.* (2022):

$$\mathcal{D}_e = \kappa h_L \nabla_c^2 c_L - \chi \cdot h_L \nabla_c c_L, \quad (3.6)$$

where κ is an isotropic eddy diffusivity and χ is an eddy-induced velocity (EIV). Lu *et al.* (2022) showed that this formulation can accurately reproduce the eddy-induced advection in a high-resolution model. Here, we use this approach to explore the advective effects of eddies on front evolution.

In frontal zones, the advective velocities \mathbf{u}_L and χ tend to be strong and nearly parallel to large-scale tracer contours whereas only their components that are perpendicular to the tracer contours are significant for tracer distribution. We, therefore, introduce here “effective eddy-induced velocity” or EEIV. EEIV is conceptually analogous to the “effective diffusivity” (e.g. Nakamura 1996) since it is also applied on the direction perpendicular to the tracer contours. We will later demonstrate that this scalar formulation has several advantages over using the vector χ . We will later also use a similarly defined effective large-scale velocity (ELSV).

316 Equation (3.6) then becomes

$$\hat{\mathcal{D}}_e(\kappa, \chi_\perp; c_L) = \kappa h_L \nabla_c^2 c_L - \chi_\perp |h_L \nabla_c c_L| \delta_c, \quad (3.7)$$

318 where the EEIV $\chi_{\perp} = \chi \cdot n \delta_c$, n is the unit vector along tracer gradient $n =$
 319 $h_L \nabla_c c_L / |h_L \nabla_c c_L|$, and δ_c is a sign function depending on the direction of the zonal-

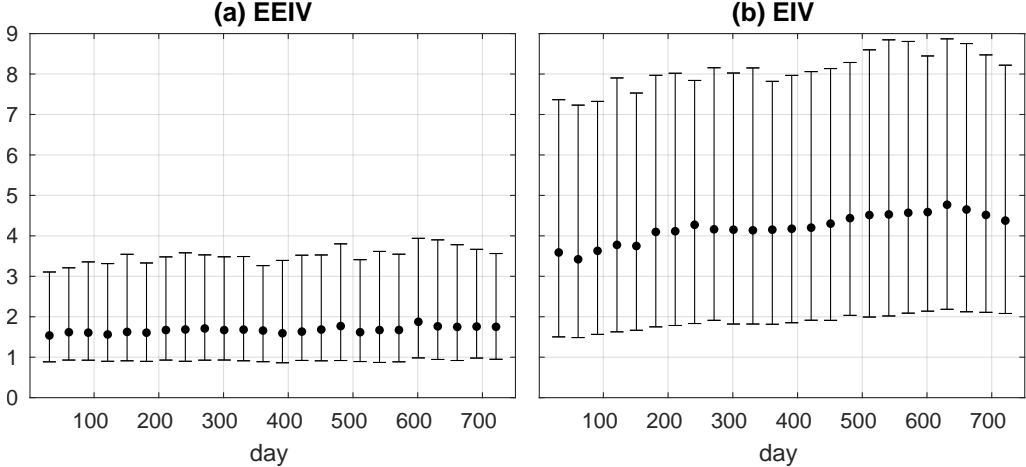


Figure 6: Tracer dependence, calculated as a ratio of the standard deviation to the absolute ensemble mean, of (a) EEIV χ_{\perp} and (b) EIV χ . Error bars denote the median and the 25–75th percentile range of the ratio. The ensemble of EEIV includes 10 estimates diagnosed from 10 (passive temperature tracer, chemical tracer and eight idealized tracers) tracers. The ensemble of EIV includes 10 estimates randomly chosen from all the 45 estimates (45 tracer pairs generated from 10 tracers). For EIV, the ratios of its two horizontal components are averaged. Data are in the upper layer.

320 mean meridional tracer gradient:

$$321 \quad \delta_c = \begin{cases} 1, & \frac{\overline{h_L \partial_y c_L}}{x} > 0 \\ -1, & \frac{\overline{h_L \partial_y c_L}}{x} < 0. \end{cases} \quad (3.8)$$

322 The function is introduced to simplify interpretation of the scalar χ_{\perp} and eliminates its
323 dependence on the direction of the large-scale tracer gradient. For example, a northward EIV
324 χ has a positive projection ($\chi \cdot \mathbf{n} > 0$) onto a front with northward tracer gradient ($\delta_c = 1$)
325 but has a negative one onto a front with southward gradient ($\delta_c = -1$). By multiplying by δ_c ,
326 χ_{\perp} becomes positive in both cases and can be interpreted as speed at which eddies displace
327 tracer contours.

328 Note that using the advective approach has clear advantages in this study focused on
329 eddy-driven frontogenesis, since this is a fundamentally non-diffusive process (McWilliams
330 2021). Although, technically speaking, gradient sharpening can be achieved by negative
331 diffusivity, its practical implementation causes numerical instability in models (Trias *et al.*
332 2020; Kamenkovich *et al.* 2021; Lu *et al.* 2022). Diffusive effects of eddies expressed via
333 κ , however, can be important in the oceanic interior. Therefore, we set the eddy diffusivity
334 κ as a positive constant $\kappa = 400 \text{ m}^2 \text{ s}^{-1}$, which is an estimate of the domain-mean κ in the
335 upper layer. The unknown, χ_{\perp} , is calculated by inverting (3.7) with the diagnosed \mathcal{D}_e on the
336 left-hand side and c_L being the tracer solution of the W_EF simulation. For comparison, the
337 vector EIV χ is also calculated by inverting (3.6) using two tracers (two equations). More
338 details of the inversion can be found in Haigh *et al.* (2020) and Lu *et al.* (2022).

339 One of the advantages of the scalar formulation (3.7) over the vector formulation (3.6) is
340 the reduction of tracer dependence. The tracer dependence refers to the sensitivity of EEIV
341 χ_{\perp} or EIV χ to the initial tracer distributions and was reported for eddy diffusivity and
342 eddy transport tensor (Bachman *et al.* 2015; Haigh *et al.* 2020; Kamenkovich *et al.* 2021;
343 Sun *et al.* 2021; Lu *et al.* 2022). In theory, the eddy diffusivity and the (E)EIV are assumed
344 to be quantities inherent to the eddy flow and independent of the tracer itself. The tracer

dependence, therefore, contradicts this fundamental assumption and implies potential bias in representing eddy effects using these quantities. For example, Lu *et al.* (2022) showed that χ is less tracer dependent than the eddy diffusivity, which is interpreted as advantage of the advective formulation. Here we calculate the tracer dependence in the same way as Lu *et al.* (2022). We first calculate an ensemble of χ_{\perp} (χ) from a set of tracers (tracer pairs). The tracer dependence is then defined as the ratio of the ensemble standard deviation to the absolute ensemble mean of χ_{\perp} (χ). Figure 6 compares the ratios for χ_{\perp} and χ . We see that the tracer dependence of χ_{\perp} is significantly reduced compared to that of χ . Our additional analysis further shows that the sign function δ_c (3.8) is important for the reduction in tracer sensitivity. These results demonstrate the benefit of using the EEIV to represent the eddy effects.

The conservation of global tracer inventory when applying the EEIV formulation (3.7) is enforced using the method in Lu *et al.* (2022). A correction is added to the parameterized eddy forcing $\hat{\mathcal{D}}_e$, that makes its global integral zero in the closed domain. The correction is conceptually similar to the conservation enforcement widely used in stochastic parameterizations (Leutbecher 2017). We describe it and confirm the conservation in Appendix E.

362 4. Effect of eddies on the front

363 In this section, we explore the role of eddies in the frontal evolution by analyzing the tracer
 364 distribution and the frontogenesis equation in our numerical experiments. We only show the
 365 results for the passive temperature tracer but confirm that all conclusions remain the same
 366 for the chemical tracer as well.

367 4.1. Analysis of the frontogenesis equation

368 To examine how eddies interact with large-scale flow in sharpening the front, we study the
 369 frontogenesis equation (3.5) for the W_EF experiment. Figure 7a shows the time series of
 370 all terms in the budget averaged within the EJE region. The tendency term fluctuates around
 371 zero after the tracer is stirred up, showing that a statistically steady state of tracer is reached.
 372 Several important points are drawn from the budget. Firstly, the area-mean eddy term E
 373 remains positive, meaning that it acts to increase the magnitude of tracer gradients. This
 374 implies that eddies are sharpening the front, which agrees with the previous comparison
 375 between the NO_EF and W_EF simulations. In contrast, the effect of large-scale current,
 376 characterized by the negative L term of similar magnitude with E , is to weaken the front.
 377 There is also a large inverse spatial correlation of -0.9 between L and E , meaning that the
 378 large-scale and eddies are acting to balance each other in the front evolution. The residual
 379 (sum) of the two is at least one order of magnitude smaller than any of the terms and
 380 is balanced by the sum of the (squared) tracer gradient tendency, the diffusion A and the
 381 relaxation R . The diffusion remains negative and acts to reduce the magnitude of the front as
 382 anticipated. The relaxation has a very small magnitude and helps sustain the front. Figure 7b
 383 further shows the two components of L , both representing effects of the large-scale advection.
 384 The large-scale velocity confluence term L_{con} plays a dominant role in the weakening of
 385 the front, while the advection term L_{adv} occasionally counteracts L_{con} with a much smaller
 386 magnitude. The small magnitude of L_{adv} could be explained by the fact that the large-scale
 387 flow \mathbf{u}_L in EJE is nearly perpendicular to the gradient of the squared tracer gradient.

388 To further explore the relationship between large-scale and eddy effects on the front, we
 389 compute the point-wise time correlations between the frontogenetic budget terms (figure
 390 8). We see that large negative correlations between L and E are concentrated along the
 391 EJE, indicating strong mutual compensation between the large- and mesoscale processes in

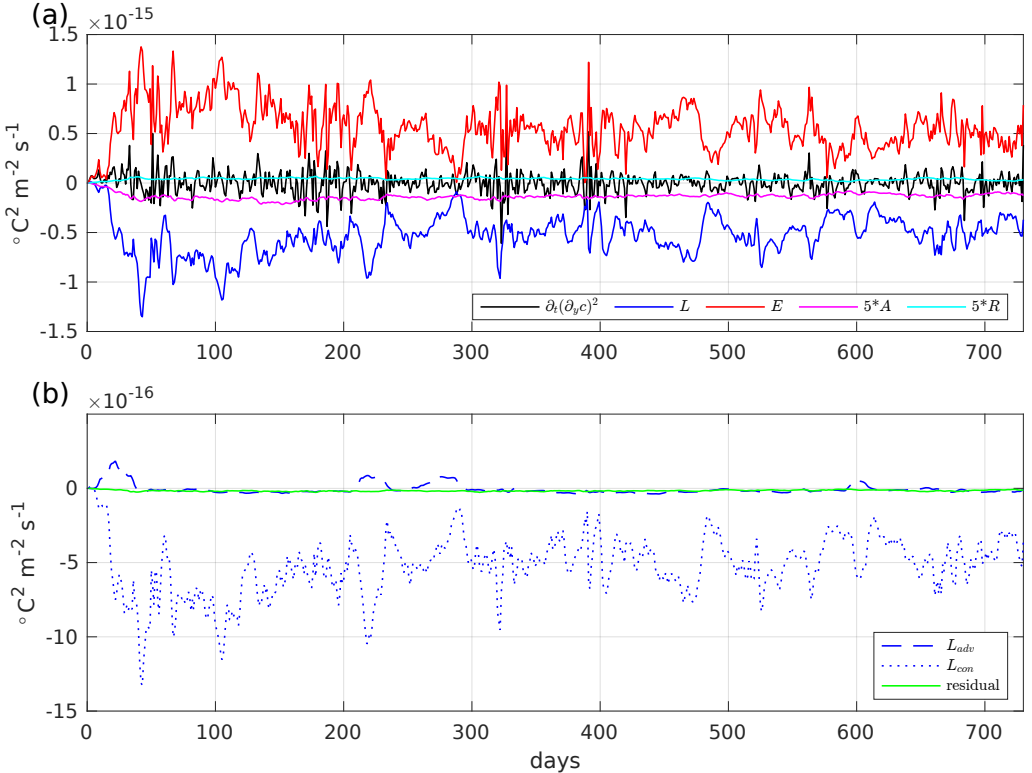


Figure 7: Time series of terms in the frontogenesis equation averaged in the EJE region (defined in Figure 5). (a) The tendency, L , E , A and R (A and R are multiplied by a factor of 5) terms. (b) The two components of L : L_{adv} and L_{con} , and the residual of the budget. Results are for the passive temperature tracer in the upper layer.

392 the region, where the eddy forcing is also particularly large (figure 4a-b). This correlation
 393 suggests a possibility of a potential closure for the EEIV χ_\perp in terms of the large-scale
 394 fields, that will be discussed in the next section. The tendency term in the jet region is not
 395 significantly correlated to either L or E alone, because the gradient is governed by the joint
 396 effect of large-scale and eddies, as indicated by the area-mean budget (time series). Outside
 397 of the jet region, the tendency is stronger correlated to E than L , which is likely due to
 398 the transient eddy effect on tracer contours. However, since the tracer concentrations there
 399 are not significantly different between the NO_EF and W_EF simulations and that our main
 400 focus is on the frontal region, we do not discuss the effect of eddies outside of the jet region.
 401 We also see that E is mainly negatively correlated with L_{con} rather than L_{adv} along the jet,
 402 re-confirming the dominant role of L_{con} in the large-scale flow effect.

403 4.2. Importance of the eddy-induced advection

404 Our results have so far demonstrated that mesoscale eddies sharpen the front while the large-
 405 scale flow plays an opposite role. We next use the concept of eddy-induced advection to
 406 demonstrate the compensation between eddies and large-scale currents. Note that the same
 407 analysis would be significantly less straightforward if the diffusivity tensor with negative
 408 diffusivities were used, because perfect compensation between advection and diffusion cannot
 409 be achieved for an arbitrary tracer. Figure 9 shows the standard deviation, time-mean and
 410 zonal-mean of the EEIV χ_\perp , as well as the effective large-scale velocity (ELSV) $\mathbf{u} \cdot \mathbf{n} \delta_c$

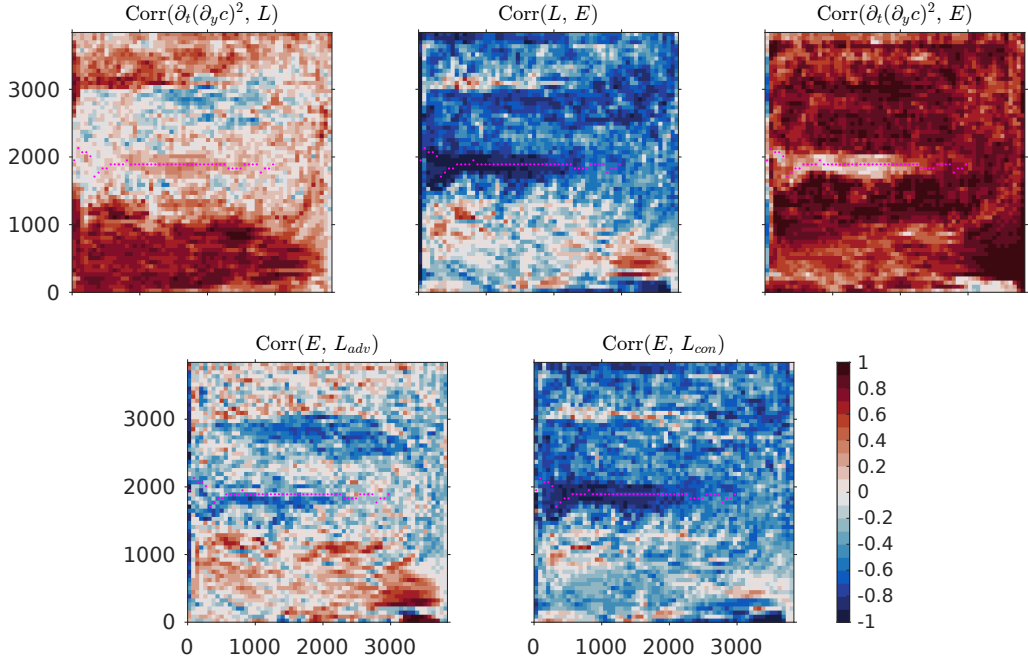


Figure 8: Pointwise time correlations between different terms in the frontogenesis equation over 2 years in the upper layer. Magenta dots are the EJE core.

for the passive temperature tracer. In general, χ_\perp and u_\perp have the same order of magnitude, showing their equally important roles in tracer distributions. The std of χ_\perp exceeds its time mean and concentrates along the jet, indicating a large time variability as the eddy forcing. The time-mean χ_\perp is mostly negative (positive) at the north (south) of the core, which cools (warms) the cold (warm) water by imposing negative (positive) eddy forcing (figure 9b-c). The total effect is to amplify the negative gradient and sharpen the temperature front. The sign of χ_\perp also indicates that the EIV χ across tracer contours at the north (south) of the EJE core is directed mainly southward (northward). That is, physically, the EIVs on both sides of the EJE squeeze the temperature contours together by bringing cold and warm water towards each other, thus sharpening the front. The eddy-induced squeezing of tracer contours has been reported by many studies in terms of up-gradient eddy-induced diffusion (Kamenkovich *et al.* 2021; Haigh *et al.* 2021a; Haigh & Berloff 2021). Here, it is effectively quantified by the eddy-induced advection. The ELSV u_\perp has an opposite profile to χ_\perp in the EJE region (figure 9f), confirming the compensation between the two as discussed above.

5. Simulation of the front in coarse-resolution tracer model

The goal of this section is to explore parameterization of the tracer eddy forcing \mathcal{D}_e using the EEIV χ_\perp , i.e., let $\mathcal{D} = \hat{\mathcal{D}}_e(\chi_\perp; c_L)$ in (2.3). We will evaluate the skill of the EEIV χ_\perp in simulating the eddy-driven sharpening of the front and will propose a simple closure for its parameterization.

5.1. Loss of skill for exact parameters

Our first step toward parameterization is to apply the exactly fitted EEIV χ_\perp in the tracer simulation, using the tracer concentrations c_L taken from the W_EF simulation. We denote this experiment as EXACT_EEIV. The exact χ_\perp is calculated by inverting (3.7) for the passive

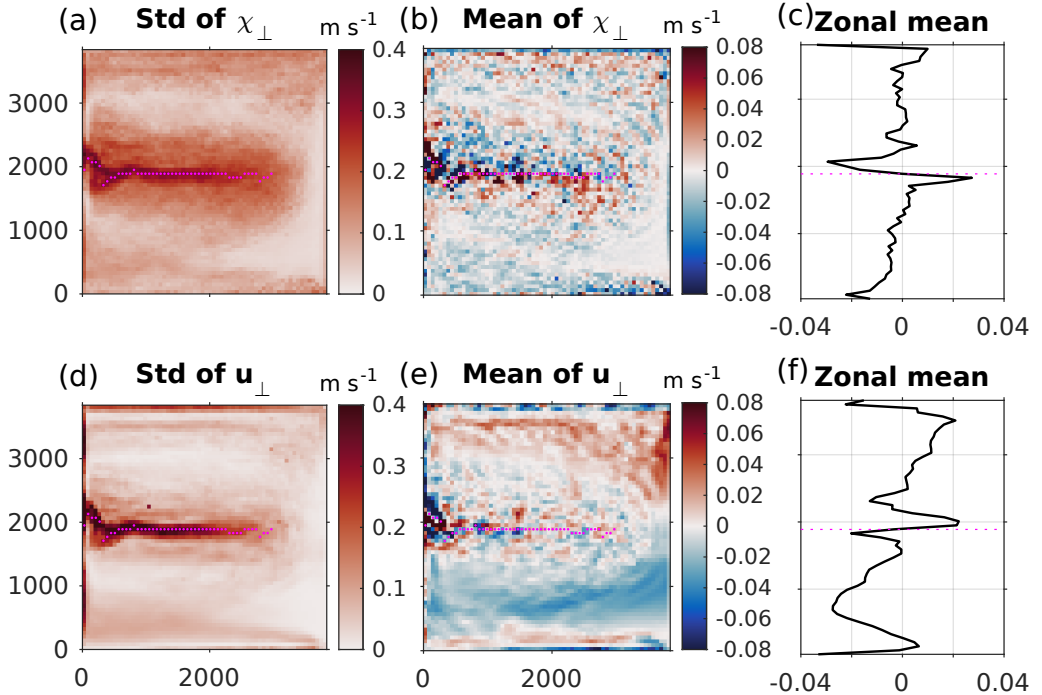


Figure 9: (a) The standard deviation, (b) time mean and (c) time- & zonal-mean of the EEIV χ_{\perp} . (d)-(f) Same but for ELSV u_{\perp} . Both are projected onto the passive temperature tracer. The data is over year 21-22. Magenta dots in color plots are the EJE core. Magenta dotted line in (c) and (f) shows the zonal-mean latitude of the EJE core. Outliers in χ_{\perp} that fall below 1% percentile or above 99% percentile are excluded for presentation purposes.

temperature tracer. It should, in theory, be able to accurately reproduce \mathcal{D}_e and the tracer concentration in W_EF. We, however, found large biases in the resulting solution. Figures 10a-c show the temperature solution in the EXACT_EEIV and time series of the meridional gradients defined in figure 5. Compared to W_EF (figure 5), the tracer has a large bias near the EJE core. Interestingly, the front becomes even weaker than in the NO_EF simulation, as evidenced by the tracer gradients (figures 10b-c to figures 5e-f). This shows a loss of skill of the exact χ_{\perp} in the jet extension region. In the rest of the domain the solution in EXACT_EEIV is visually indistinguishable from W_EF. However, the eddies there have relatively small effects on the large-scale tracer distribution, and our goal is not to reproduce individual features in the interior of the subtropical gyre.

The fact that the exact χ_{\perp} fails to reproduce a correct EJE front is likely due to the deterioration of the spatiotemporal co-variability of the front position and eddy forcing. The tracer front constantly changes its position due to the large-scale-eddy interaction, and the corresponding eddy forcing \mathcal{D}_e and χ_{\perp} both have complex spatiotemporal dependence (figure 4a-c; figure 9a-b) that is closely related to the frontal evolution. Thus, to accurately reproduce the front, the parameterized eddy forcing $\hat{\mathcal{D}}_e(\chi_{\perp}; c_L)$ should capture this coupling with the front in both space and time. This is clearly a hard task because even a small error in the runtime solution c_L can cause an error in the eddy forcing $\hat{\mathcal{D}}_e$, and induce an error in the coupling between the front and $\hat{\mathcal{D}}_e$. The errors in the forcing can grow very fast due to chaotic sensitivity. For example, a bias in the eddy forcing can cause cooling in places where warming is needed for sharpening the front, which in turn amplifies errors in the solution.

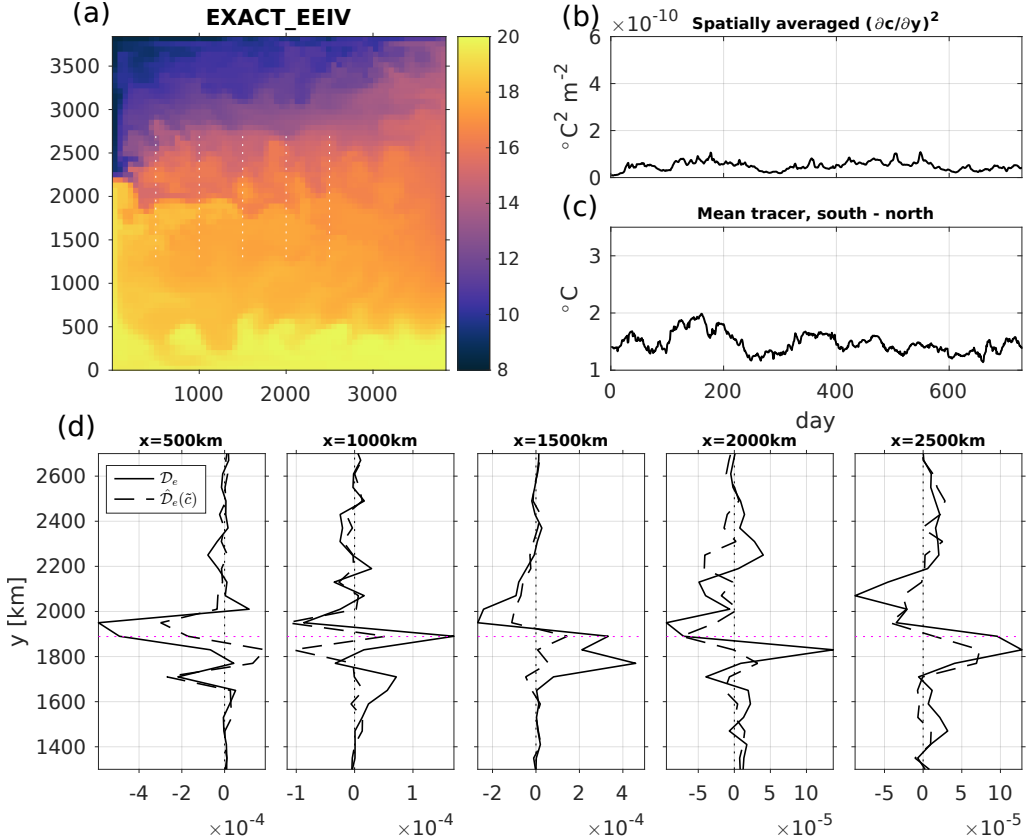


Figure 10: Passive temperature solution ($[^{\circ}\text{C}]$) in the EXACT_EEIV simulation. (a) Snapshot at day 361 year 21. (b)-(c) The spatial averaged squared meridional tracer gradient and the tracer difference between the south and north of the EJE, respectively, as functions of time (same as in figures 5e-f). (d) Meridional profiles of the true eddy forcing \mathcal{D}_e and the parameterized eddy forcing $\hat{\mathcal{D}}_e(\chi_{\perp}; c_L)$ diagnosed in the EXACT_EEIV run, at different longitudes shown by the white dots in (a). Magenta dots denote the latitudes of the EJE core.

455 Figure 10d compares several meridional sections of time averaged $\hat{\mathcal{D}}_e(\chi_{\perp}; c_L)$ and original
 456 full \mathcal{D}_e . We see that $\hat{\mathcal{D}}_e$ is generally much smaller than \mathcal{D}_e around the front ($1600 \text{ km} < y <$
 457 2400 km), and thus produces a much weaker front despite having “perfect” χ_{\perp} . The eddy
 458 forcing is close to zero in the rest of the domain, where eddy activities are weak, showing
 459 that the tracer bias is concentrated in the front region of strong eddy effects. In the following
 460 section, we will see that an idealized, time-independent profile for χ_{\perp} will be more efficient
 461 in representing effects of eddies on the front.

462 5.2. A simplified EEIV and its performance in simulations

463 In the previous section, we observed that time varying, two-dimensional EEIV χ_{\perp} aggravates
 464 biases in the simulation, and suspect that this complexity is the cause of the problem. Small
 465 errors in tracer distribution can lead to positive feedback and further error amplification.
 466 This can happen if an important correlation between two complex fields, χ_{\perp} and c_L , is
 467 broken. To evaluate this hypothesis, we consider here a highly idealized χ_{\perp} profile designed
 468 to guarantee the eddy-driven frontogenesis. If successful, this simple model can pave way to
 469 parameterization of the process. The most straightforward choice is a time-independent and

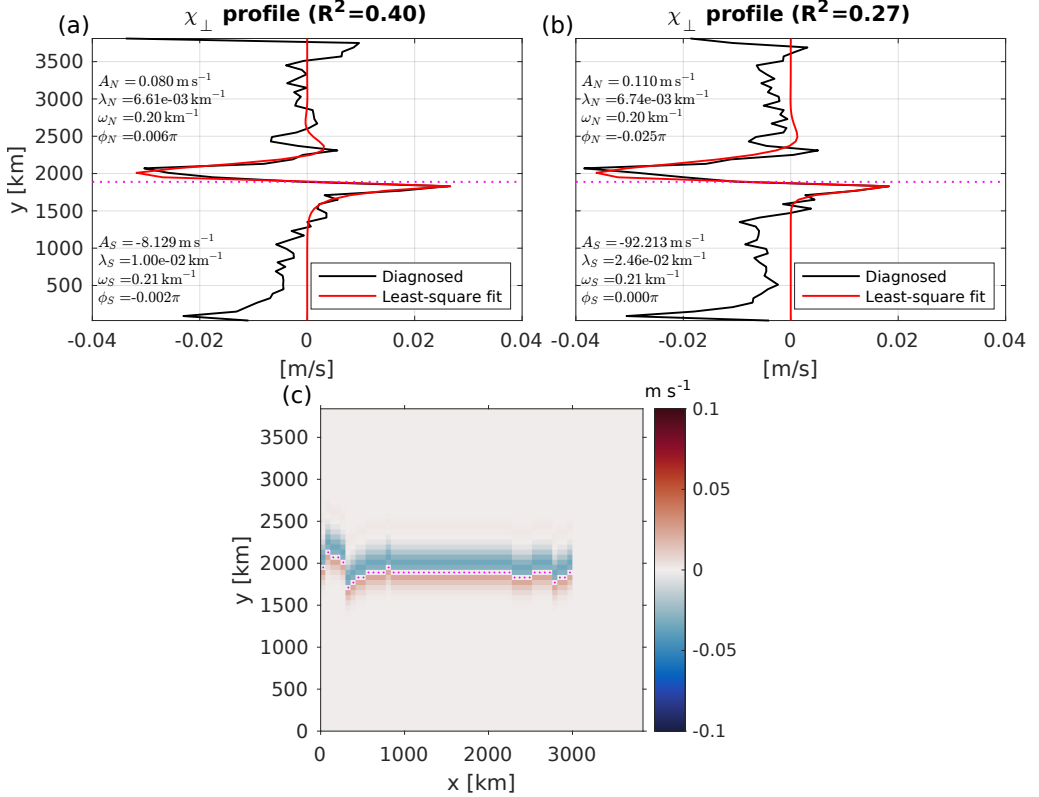


Figure 11: Meridional profiles fitted from the time- and zonal-mean EEIV χ_{\perp} diagnosed from the (a) passive temperature and (b) chemical tracers. The time mean is calculated over 2 years. (c) 2D χ_{\perp} field generated from the fitted profiles in (a) and (b). Magenta dots are EJE core.

zonally uniform profile. We have seen in figure 9b-c that χ_{\perp} is zero at the EJE core, rapidly grows to a large negative (positive) value in the north (south) and then decays away from the core. We fit this time- and zonal-mean profile of χ_{\perp} in a least-square sense by a simple damped sinusoidal function:

$$\hat{\chi}_{\perp}(y) = \begin{cases} A_N e^{-\lambda_N(y-y_{GS})} \sin(\omega_N(y - y_{GS}) + \phi_N), & y > y_{GS} \\ A_S e^{-\lambda_S(y_{GS}-y)} \sin(\omega_S(y_{GS} - y) + \phi_S), & y < y_{GS} \end{cases} \quad (5.1)$$

where y_{GS} is the latitude of the jet core, subscripts N and S denote the parameters of the sinusoidal function in the north and south of the core, respectively. The χ_{\perp} profiles and fitted functions $\hat{\chi}_{\perp}(y)$ for the passive temperature and chemical tracers are shown in figures 11a-b. The two tracers, although having very different initial meridional distributions, give similar profiles of χ_{\perp} . This is another manifestation of a modest tracer dependence in EEIV, as discussed in section 3. We then calculate an idealized 2D χ_{\perp} field from the fitted profiles as follows. At each longitude, χ_{\perp} is given by $\hat{\chi}_{\perp}(y)$ with y_{GS} being the latitude of the jet core at that longitude. The resulting χ_{\perp} fields from the two tracers are then averaged to generate the desired idealized χ_{\perp} field, as shown in figure 11c.

We next use the derived idealized field of the EEIV to simulate the passive temperature and chemical tracers on the coarse grid. We denote these experiments as IDL_EEIV. The strength of the front is measured here by the difference of the spatially averaged tracers on

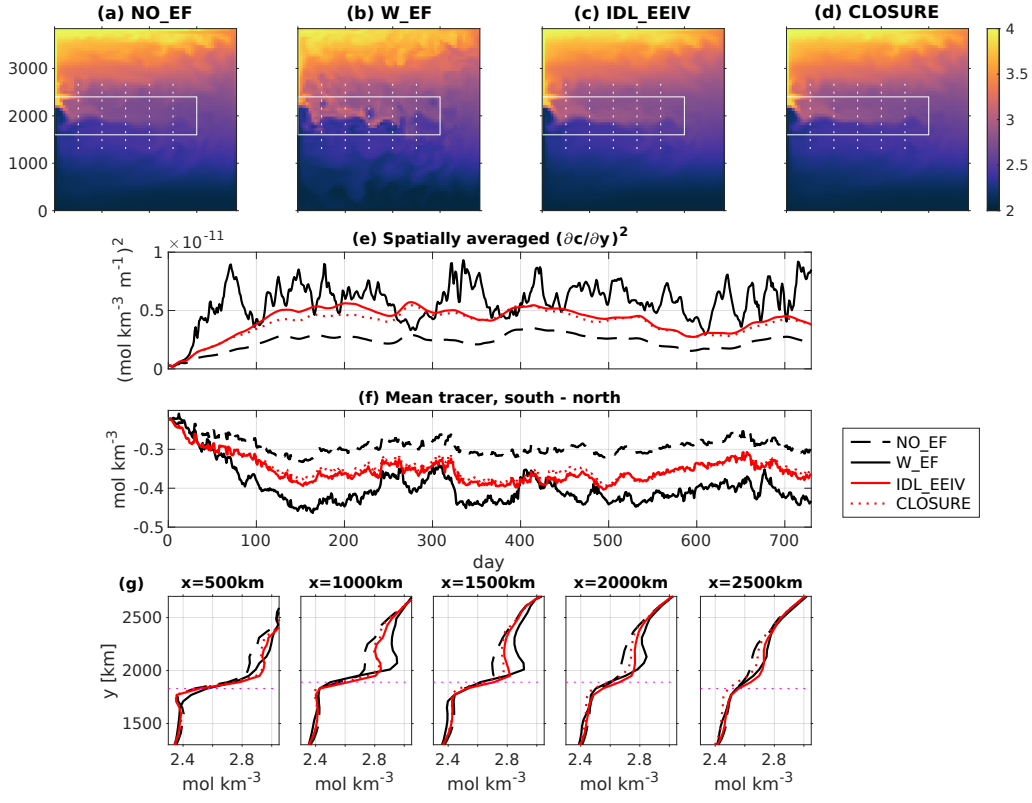


Figure 12: Same as Figure 5 but for the chemical tracer.

487 the two sides of EJE. Figure 5 shows the passive temperature solution and its gradient from
 488 the IDL_EEIV experiment in comparison to those from NO_EF and W_EF. We now see that
 489 the strong temperature gradients along the EJE and in the surrounding area are reproduced
 490 well by the idealized χ_\perp after the first 200 days (figure 5e-f). The meridional profiles further
 491 show that the meridional gradients across the EJE (figure 5g) improve relative to the NO_EF
 492 values, despite a small remaining bias in the position of the front, possibly caused by time
 493 dependence in the EJE position. The improvement in the simulation of the temperature
 494 front over the NO_EF case is expected since the forcing is designed to bring warm (cold)
 495 water to the south (north) of the EJE. This result is a clear demonstration of the advantage
 496 of using eddy advection over the eddy diffusion and an idealized EEIV profile over the 2D
 497 time-dependent EEIV, in representing the eddy-driven sharpening of front. The sharpening is
 498 relatively straightforward to enforce in our χ_\perp formulation, whereas it cannot be guaranteed
 499 by the vector χ , which is nearly parallel to the tracer contour, and, of course, cannot be
 500 achieved by positive diffusion.

501 Simulations of the chemical tracer with the same χ_\perp give similar results (figure 12),
 502 demonstrating a robustness of the formulation. The southward meridional tracer gradient in
 503 W_EF is 30% larger than in NO_EF, and our idealized χ_\perp can increase the magnitude of
 504 the gradient in NO_EF by about 15% (figure 12f). The slightly reduced skill in this case
 505 compared to the temperature simulation is due to the tracer dependence: the χ_\perp diagnosed
 506 from the chemical tracer is slightly larger than the one from the temperature tracer in the
 507 north of the EJE (figure 11a-b). As a result, it leads to a weaker eddy forcing.

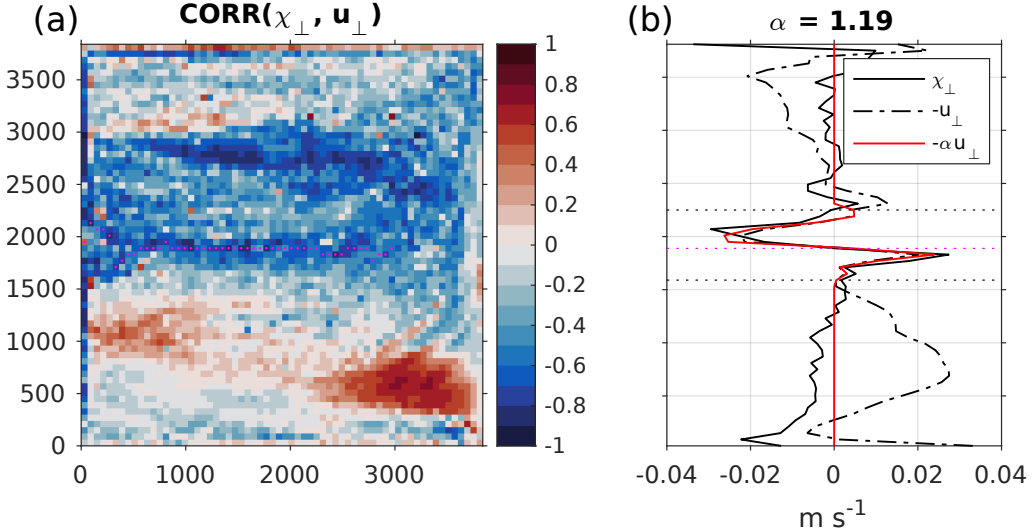


Figure 13: (a) Correlation between χ_{\perp} and u_{\perp} over 2 years in the upper layer. (b) Meridional profiles of the time- and zonal-mean χ_{\perp} (black solid) and minus u_{\perp} (dot dash). Horizontal black dots show latitudes of the data from which α is estimated. Magenta dots are the EJE core. Red solid line is the predicted χ_{\perp} by the fitted α and u_{\perp} profile.

508

5.3. Closure of EEIV by the large-scale flow

509 As the last step, we propose a closure for EEIV χ_{\perp} in terms of large-scale fields on the
 510 coarse grid. We have seen that the time- and zonal-averaged χ_{\perp} and ELSV u_{\perp} have similar
 511 but opposing profiles within the latitudes of EJE (figures 9c,f). Figure 13a further shows
 512 significant negative correlation between the two fields around the jet; some positive values
 513 are, however, visible in the southern domain where the tracer is nearly uniform and is of little
 514 interest. This is also consistent with the correlation between the large-scale and eddy terms
 515 in the frontogenesis equation (figure 8). These results suggests a possibility that χ_{\perp} can be
 516 expressed linearly by u_{\perp}

517

$$\chi_{\perp} = -\alpha u_{\perp}, \quad (5.2)$$

518 where the coefficient α quantifies the balance between the two.

519 We next implement this closure in the tracer model by substituting it for χ_{\perp} in (3.7). To
 520 reduce the errors that could be caused by the variability in χ_{\perp} as discussed above, we ignore
 521 the temporal and zonal variability in χ_{\perp} and choose to predict an 1D profile:

522

$$\chi_{\perp}(y) = -\alpha \bar{u}_{\perp}^{xt}(y), \quad (5.3)$$

523 where $\bar{u}_{\perp}^{xt}(y)$ is the zonal and 2-year time mean ELSV. The predicted $\chi_{\perp}(y)$ will be extended
 524 to 2D by mapping at each longitude as previously done. The resulting 2D field will be applied
 525 to the model. Since the significant correlation between χ_{\perp} and u_{\perp} is concentrated in the EJE
 526 region, we estimate α by minimizing the RMS error between the two profiles in the latitudes
 527 of EJE. The parameterized χ_{\perp} is shown in figure 13b. The coefficient α has a value of about
 528 1.2, indicating a dominating role of eddy-induced advection in balancing the large-scale
 529 advection. Note that the value is different from unity, meaning the compensation between
 530 EEIV and ELSV is not complete. Also note that this α quantifies the time- and zonal mean
 531 relation between the two, and the instantaneous relation can be different. In fact, a pointwise
 532 regression of χ_{\perp} on u_{\perp} resulted in a space-dependent coefficient (not shown) that ranges
 533 from -1 to -0.4 in the EJE region, indicating a partial balance in most places.

534 For practical applications, the coefficient α is not known a priori and has to be chosen as
 535 part of model “tuning”. For example, our attempt to implement the above closure showed that
 536 the empirical value of 1.2 is not sufficient to reproduce a sharp front. We then tested a set of
 537 α and found that the magnitude of the front increases with larger α . This is expected because
 538 α controls the magnitude of the EEIV and tracer eddy forcing (3.7), thus affecting the front
 539 sharpness. This closure is similar to the amplification of the eddy backscatter proposed by
 540 Berloff (2018), which aims to parameterize the dynamic eddy effects on the EJE, whereas
 541 our closure aims at the eddy effects on tracer front.

542 Here we report the result of the test with $\alpha = 2$ (denoted as “CLOSURE”) for the passive
 543 temperature and chemical tracers in figure 5 and 12, respectively. The closure reproduces
 544 a sharp front for both tracers as effectively as the IDL_EEIV simulation, indicating that it
 545 could be a promising parameterization of the eddy-driven frontogenesis. Note that the value
 546 of α possibly depends on the flow properties, e.g. the interaction between large-scale and
 547 eddies in front evolution, and thus needs to be carefully selected in different models and/or
 548 flow regimes.

549 6. Conclusions and discussion

550 This study investigates the importance of mesoscale eddies in the formation and evolution of
 551 large-scale oceanic tracer fronts along the eastward jet extension (EJE) of western boundary
 552 currents. Using an idealized eddy-resolving model of the double gyre system, we quantify the
 553 effects of eddies using the tracer “eddy forcing” on the coarse-resolution grid. As discussed
 554 by several previous studies, this approach has advantages over methods based on eddy
 555 fluxes, both because it incorporates all eddy terms in the tracer budget and because it
 556 avoids ambiguity associated with large non-divergent (“rotational”) fluxes (Haigh *et al.*
 557 2020; Kamenkovich *et al.* 2021; Lu *et al.* 2022). If the eddy forcing is simulated correctly
 558 in the coarse-resolution simulations, one can hope that the tracer field can be simulated
 559 accurately as well. This study focuses on the eddy-induced stirring of tracers, whereas the
 560 contribution of eddies to momentum and mass/density fluxes are outside its scope.

561 The key result is that mesoscale eddies sharpen the large-scale tracer front, as demonstrated
 562 by both the sensitivity tracer experiments in an offline model and the frontogenesis equation.
 563 This is manifested by a significantly sharper front in the simulation with the eddy forcing than
 564 in the run without, despite the mass fluxes being the same in both simulations. The analysis
 565 of the terms in the frontogenesis equation confirms this conclusion, and further shows that
 566 the large-scale current counteracts the eddy-driven frontogenesis, nearly compensating it in
 567 a steady state. The confluence (strain) of the large-scale velocity, rather than the large-scale
 568 advection of tracer gradients, plays a major role in the latter effect.

569 The frontal sharpening by eddies and mutual compensation of eddy-driven and large-scale
 570 advections in the frontogenesis can be conveniently quantified using a recently proposed
 571 generalized advective framework (Lu *et al.* 2022). In this study, we further modify this
 572 approach by using an effective eddy-induced velocity (EEIV, a scalar χ_{\perp}), which is a speed
 573 with which eddies advect large-scale tracer contours. The EEIV effectively describes the
 574 mechanism of the eddy-driven frontogenesis: taking the passive temperature as an example,
 575 the eddies facilitate the advection of warmer (colder) water to the warm (cold) side of
 576 the front, squeeze the tracer contours, and thus sharpen the front. The same process is
 577 challenging to describe by eddy diffusion. For example, recent studies (Kamenkovich *et al.*
 578 2021; Haigh *et al.* 2021a; Haigh & Berloff 2021) have found persistence of pairs of
 579 positive and negative eddy diffusivities (“polarity”) that could be potentially responsible
 580 for stretching the contours and producing tracer filaments or fronts (Haigh & Berloff 2022).
 581 However, negative diffusivities are numerically unstable, and compensation with the large-

582 scale advection cannot be guaranteed for an arbitrary tracer. In addition, either up- or down-
 583 gradient diffusion is associated with cross-contour mixing, which is incompatible with the
 584 contour-squeezing nature of the front. Thus, we argue that an advective model is more suitable
 585 for representing the eddy-driven frontogenesis.

586 The EEIV formulation has two main advantages over the originally proposed vector
 587 formulation of the eddy-induced velocity (EIV, χ , (Lu *et al.* 2022)). The first advantage is the
 588 reduced tracer dependence, which means less sensitivity of χ_{\perp} to initial tracer profiles and
 589 thus smaller bias in simulating different tracers. Since Lu *et al.* (2022) shows a reduced tracer
 590 dependence of χ compared to the eddy diffusivity, the EEIV χ_{\perp} also has clear advantages
 591 over the diffusivity in this regard. The second advantage is that the uncovered eddy-induced
 592 frontal sharpening can be readily enforced by specifying χ_{\perp} in coarse-resolution models. Our
 593 results show that the EEIV effectively reproduces the strength of the front for both tracers
 594 with very different initial distributions: the passive temperature and chemical tracers. The
 595 EIV framework is, however, less practical because the vector χ is nearly parallel to the tracer
 596 contours in the frontal region and only a small cross-contour (effective) component of χ
 597 matters. Thus, even small errors in χ may yield large bias in the component and thus the
 598 front.

599 An interesting finding of this study is that the EEIV with full spatiotemporal variability
 600 fails to guarantee the frontogenesis and instead leads to further deterioration of the front from
 601 the simulation without eddy forcing. This is because of the rapid loss of correlation between
 602 the meandering front and parameterized eddy forcing, which leads to chaotic sensitivity
 603 of the frontal evolution to eddy forcing. The main merit of our results is that successful
 604 eddy tracer parameterization can be achieved with simplified, rather than most complex,
 605 parameterization, as long as the most important properties of the eddy effects can be
 606 preserved. For example, in this study, the tracer front is formed by the squeezing of the
 607 near-zonal tracer contours by the EIVs in the north and south of the EJE. We managed
 608 to use a simplified profile of EEIV to capture this feature of EIV that matters for fronts
 609 and thus guaranteed the frontogenesis. However, identification of such essential features
 610 may not be always straightforward since it requires careful analysis of what properties
 611 (e.g. spatiotemporal structures) of eddy effects are most important for the specific ocean
 612 phenomenon of interest. Machine learning approaches can be promising in this regard since
 613 they can extract essential properties from complex fields and even discover new physical
 614 relations (Zanna & Bolton 2020; Partee *et al.* 2022; Ross *et al.* 2023).

615 To account for the partial compensation between eddy-driven and large-scale tracer
 616 advection in the frontal region, we propose a closure for EEIV by using the effective
 617 large-scale velocity (ELSV). The closure captures the partial balance between EEIV and
 618 ELSV in the frontal region: the EEIV sharpens the front while the ELSV tries to broaden it,
 619 and effectively reproduces the eddy-driven frontal sharpening in the tracer experiment. The
 620 coefficient in the closure, which quantifies the compensation, is likely to depend on the flow
 621 properties. Thus, for each implementation in a model, such as a general circulation model
 622 (OGCM), one will need to tune the coefficient to produce a reasonable ocean fronts in the
 623 specific flow. Systematic investigation of the turning is left for future work.

624 Note, however, that the closure is not a complete parameterization because the large-scale
 625 flow in this study is projected from the eddy-resolving flow, with eddy-driven momentum and
 626 mass fluxes, rather than simulated in the non-eddy-resolving model. The advantage of using
 627 this approach is that we can focus on the role of tracer eddy forcing without the ambiguity
 628 from biases in momentum and mass fluxes. The dynamic effects of eddies in the EJE region
 629 is very likely to be at least as important as the eddy forcing, because the flow resolved in a
 630 non-eddy-resolving model differs significantly from the projected one, as shown in figure 3.
 631 Progress has been made in understanding and representing this dynamic effect (e.g. Berloff

632 2005; Zanna *et al.* 2017; Berloff 2018; Guillaumin & Zanna 2021; Uchida *et al.* 2022), which
633 is outside the scope of this study.

634 This study focuses on the significance of mesoscale eddies on the large-scale tracer front.
635 Submesoscale currents, another key component of oceanic flows but missing in this study, can
636 also contribute to the frontogenesis (McWilliams 2016). These three-dimensional currents
637 usually manifest themselves as overturning cells associated with upwelling and downwelling
638 that enhance the fronts in ocean surface. Note that mesoscale eddies can also induce a
639 similar overturning circulation in the surfaced mixed layer (Li *et al.* 2016; Li & Lee 2017),
640 which could be another mechanism for eddy-induced frontogenesis. The fronts characterized
641 by vertical motions occurring on horizontal scales of $O(1\text{-}10 \text{ km})$ and in the mixed layer,
642 however, are absent in our model. Studies of the importance of different scales for large-scale
643 fronts should be continued in more realistic settings, as they provide insights on frontal
644 dynamics and development of eddy parameterization scheme for non-eddy-resolving ocean
645 models.

646 **Acknowledgments.** We thank Pavel Berloff for comments on draft of this manuscript. We also thank Michael
647 Haigh for helping configure the MOM6. We acknowledge the support of the NSF Grant 1849990. We
648 acknowledge high-performance computing support from Cheyenne (doi:10.5065/D6RX99HX) and Dere-
649 cho (doi:10.5065/qx9a-pg09) provided by NCAR's Computational and Information Systems Laboratory,
650 sponsored by the NSF.

651 **Declaration of interests.** The authors report no conflict of interest.

652 **Data availability statement.** The source code of the MOM6 ocean model configured for this study
653 is available at <https://github.com/yueyanglu/MOM6-DG>. The offline tracer model source code and
654 analysis code are available at https://github.com/yueyanglu/mesoeddies_front. The offline tracer
655 model outputs and diagnostics are available at <https://doi.org/10.5281/zenodo.10005408>. The raw
656 high-resolution ocean model outputs are available upon request from the author.

657 **Author ORCIDs.** Yueyang Lu, <https://orcid.org/0000-0003-3102-8519>;
658 Igor Kamenkovich, <https://orcid.org/0000-0001-6228-5599>

659 Appendix A. Model Equations

660 Here we explain some terms in the momentum and continuity equations (2.1). More detailed
661 description of MOM6 equations can be found in Yankovsky *et al.* (2022) and Zhang *et al.*
662 (2023). The Montgomery potential M_k (2.1a) in layer k is

$$663 M_k = \sum_{i=1}^k g'_{i-1/2} \eta'_{i-1/2}, \quad (\text{A } 1)$$

where $g'_{i-1/2}$ is the reduced gravity at the upper interface of layer k and its value is prescribed
(table 1), and the upper interface height of layer k is $\eta'_{k-1/2} = -D + \sum_{i=1}^k h_i$, $D = 4 \text{ km}$ is
ocean depth. The wind stress τ is

$$\tau_x = \frac{\tau_0}{2} \left[1 + \cos \left(\frac{2\pi(mx - y + L_y/2)}{(1+m)L_y} \right) \right], \quad (\text{A } 2a)$$

$$\tau_y = m\tau_x, \quad (\text{A } 2b)$$

664 where the tilt parameter $m = 0.1$. The reference profile for the relaxation of the upper layer
665 thickness in (2.1b) is the layer thickness plus a sinusoidal function whose zero-crossing line
666 overlaps the zero wind stress curl line:

$$667 h_r = H_1 + \Delta h \sin \left(\frac{2\pi(mx - y + L_y/2)}{(1+m)L_y} \right), \quad (\text{A } 3)$$

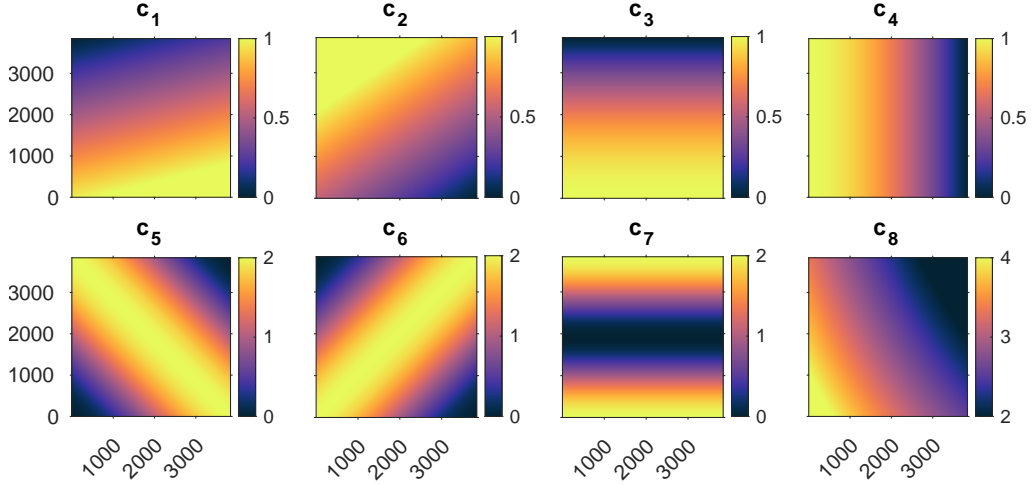


Figure 14: Initial distributions of the idealized tracers.

668 with $\Delta h = 150$ m.669 **Appendix B. Initial Distributions of Idealized Tracers**670 Besides the passive temperature and chemical tracers, this study also simulates eight
671 additional idealized tracers. They are mainly used to evaluate the tracer dependence of
672 the EEIV χ_{\perp} in section 3.3. Their concentrations are initialized with different horizontal
673 distributions and are taken constant in the vertical direction (figure 14):

$$\begin{aligned}
 674 \quad c_1 &= \frac{1}{\sqrt{17}} \left(\frac{x}{L_x} - 4 \frac{y}{L_y} + 4 \right), & c_2 &= \frac{1}{\sqrt{13}} \left(-2 \frac{x}{L_x} + 3 \frac{y}{L_y} + 2 \right), \\
 675 \quad c_3 &= \cos \frac{\pi y}{2L_y}, & c_4 &= \cos \frac{\pi x}{2L_x}, \\
 676 \quad c_5 &= -\cos \left(\frac{\pi x}{L_x} + \frac{\pi y}{L_y} \right) + 1, & c_6 &= \cos \left(-\frac{\pi x}{L_x} + \frac{\pi y}{L_y} \right) + 1, \\
 677 \quad c_7 &= \cos \frac{2\pi y}{L_y} + 1, & c_8 &= 25 * \left[\frac{\left(0.4 \frac{x}{L_x} - 1 \right)^2}{9} + \frac{\left(0.4 \frac{y}{L_y} - 1 \right)^2}{16} \right], \quad (\text{B } 1)
 \end{aligned}$$

678 where L_x and L_y are the domain sizes in the zonal and meridional directions, respectively.679 **Appendix C. Test of Offline Tracer Advection**680 To evaluate the accuracy of the offline tracer simulation, we perform both online and offline
681 simulations of the passive temperature tracer on the high-resolution grid. The tracer is
682 initialized on the first day of year 21. We use the spatial standard deviation of the tracer in a
683 model layer to quantify the error (Kamenkovich & Garraffo 2022):

$$684 \quad SD(c) = \left[\frac{1}{V} \int c^2 h dx dy - \left(\int ch dx dy \right)^2 \right]^{1/2}, \quad (\text{C } 1)$$

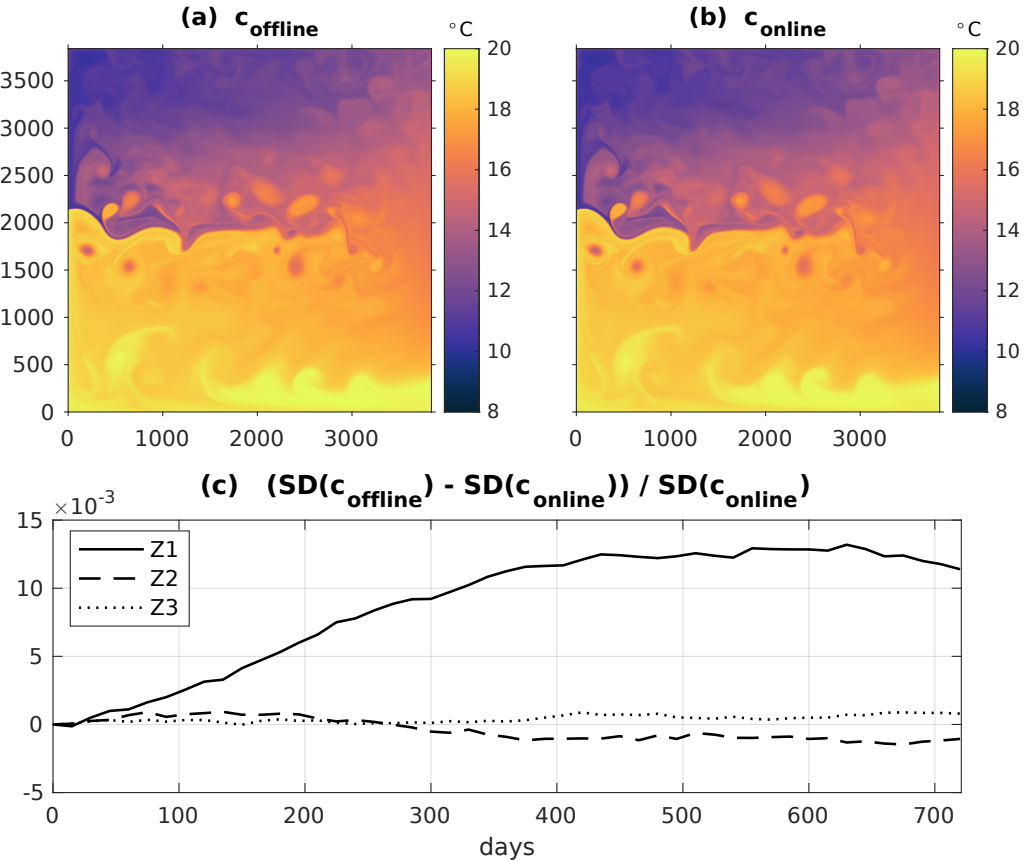


Figure 15: Passive temperature tracer solutions from the high-resolution (a) offline and (b) online simulations in the upper layer at day 365 year 22. (c) Time series of the relative bias e in the three layers.

685 where $V = \int h dx dy$ is the volume of the layer. The two solutions are indistinguishable from
 686 each other at the end of the 2-yr integration (figure 15). The relative bias, $e = (SD(c_{\text{off}}) -$
 687 $SD(c_{\text{onl}})) / SD(c_{\text{onl}})$, remain less than 1.5%. The bias is much smaller for the simulations
 688 on the coarse grid (not shown). Therefore, the errors due to the use of six-hourly mean fields
 689 are sufficiently small to warrant the use of the offline simulations.

690 Appendix D. Coarse Graining of the Mass Flux

691 The first step of defining the large-scale mass flux \mathbf{U}_L (3.3) is to coarse grain the high-
 692 resolution mass flux \mathbf{U} . Since the divergence of mass flux determines the layer thickness and
 693 thus tracer concentration, we choose to preserve the divergence during the coarse graining.
 694 This is achieved by utilizing the Helmholtz decomposition as follows. The high-resolution
 695 mass flux \mathbf{U} is first decomposed into its divergent and rotational components (Maddison *et al.*
 696 2015):

697
$$\mathbf{U} = \nabla\phi + \hat{\mathbf{z}} \times \nabla\psi, \quad (\text{D } 1)$$

698
$$\nabla \cdot \mathbf{U} = \nabla^2\phi, \quad (\hat{\mathbf{z}} \times \nabla) \cdot \mathbf{U} = \nabla^2\psi,$$

699 where ϕ is potential for the divergent component ($\nabla\phi$), ψ is streamfunction for the rotational
700 component ($\hat{z}\times\nabla\psi$), \hat{z} is the unit vector in the vertical direction, and $(\hat{z}\times\nabla)\cdot(\dots) = (-\partial_y, \partial_x)$
701 is the horizontal curl operator.

702 We then coarse grain the flux divergence to get $\langle\nabla\cdot\mathbf{U}\rangle$. To get a corresponding divergent
703 component, we solve the Poisson problem on the coarse grid with zero norm-flux boundary
704 condition

$$705 \quad \nabla_c^2\phi^c = \langle\nabla\cdot\mathbf{U}\rangle, \quad (\text{D } 2)$$

706 where ϕ_c is the potential for the divergent component ($\nabla_c\phi_c$) on the coarse grid. We also
707 coarse grain ψ to get the streamfunction for the rotational component on the coarse grid

$$708 \quad \psi_c = \langle\psi\rangle. \quad (\text{D } 3)$$

709 The coarse-grained mass flux is then defined as

$$710 \quad \langle\mathbf{U}\rangle = \nabla_c\phi_c + \hat{z}\times\nabla_c\psi_c, \quad (\text{D } 4)$$

$$711 \quad \nabla_c\cdot\langle\mathbf{U}\rangle = \nabla_c^2\phi_c = \langle\nabla\cdot\mathbf{U}\rangle, \quad (\hat{z}\times\nabla_c)\cdot\langle\mathbf{U}\rangle = \nabla_c^2\psi_c.$$

712 Its divergence by definition equals the coarse-grained divergence of the high-resolution mass
713 flux, which guarantees reasonable layer thickness and tracer solutions on the coarse grid. The
714 coarse-grained mass flux also preserves the flow structure in \mathbf{U} , because the streamfunction
715 for the rotational component of $\langle\mathbf{U}\rangle$ is directly projected from that of \mathbf{U} .

716 For a comparison, we attempted a simple way by coarse graining the zonal and meridional
717 components of \mathbf{U} separately. However, the resulting mass flux has a divergence more than ten
718 times larger than the divergence of \mathbf{U} and causes instabilities in the coarse-grid continuity
719 and tracer simulation. This issue is due to the non-commutativity between discrete spatial-
720 derivative operators and discrete coarse-graining (Mana & Zanna 2014). A more rigorous
721 divergence-preserving coarse-graining method can be found in Patching (2022) but is not
722 applied here due to its complexity.

723 The large-scale mass flux \mathbf{U}_L is then obtained by time filtering $\langle\mathbf{U}\rangle$ with a 180-day window.
724 Figure 16 shows its norm and divergence, as well as those of \mathbf{U} and $\langle\mathbf{U}\rangle$. We see that the
725 elongated jet extension is well retained in \mathbf{U}_L and the divergences of $\langle\mathbf{U}\rangle$ and \mathbf{U}_L do not exceed
726 the high-resolution flux divergence. The time filtering eliminate the mesoscale structures (e.g.
727 vortices) in $\langle\mathbf{U}\rangle$ (figures 16b-c). We conclude that the combination of coarse-graining and
728 time averaging effectively remove the mesoscale variability in the flow.

729 Appendix E. Tracer Mass Conservation

730 To ensure the tracer conservation when applying the EEIV formulation (3.7), we add a
731 correction to the local parameterized eddy forcing $\hat{\mathcal{D}}$ (Lu *et al.* 2022). The tracer solution c_*
732 at a certain time step is given by

$$733 \quad c_* = c_0 + \hat{\mathcal{D}} + w [\hat{\mathcal{D}}], \quad (\text{E } 1)$$

$$734 \quad w = -\frac{|\hat{\mathcal{D}}|}{[|\hat{\mathcal{D}}|]} \quad (\text{E } 2)$$

735 where c_0 is the tracer at the last time step, the square brackets denote a global average of
736 the layer thickness-weighted quantity: $[A] = \int Ah \, dx \, dy / \int h \, dx \, dy$, and the local weights w
737 make the magnitude of the correction proportional to the amplitude of the local eddy forcing.

738 Tracer mass conservation requires $[c_*] = [c_0]$, which is satisfied by our choice of w
739 above. One can prove this by taking $[\dots]$ of (E 1). Note that Lu *et al.* (2022) chose a simpler

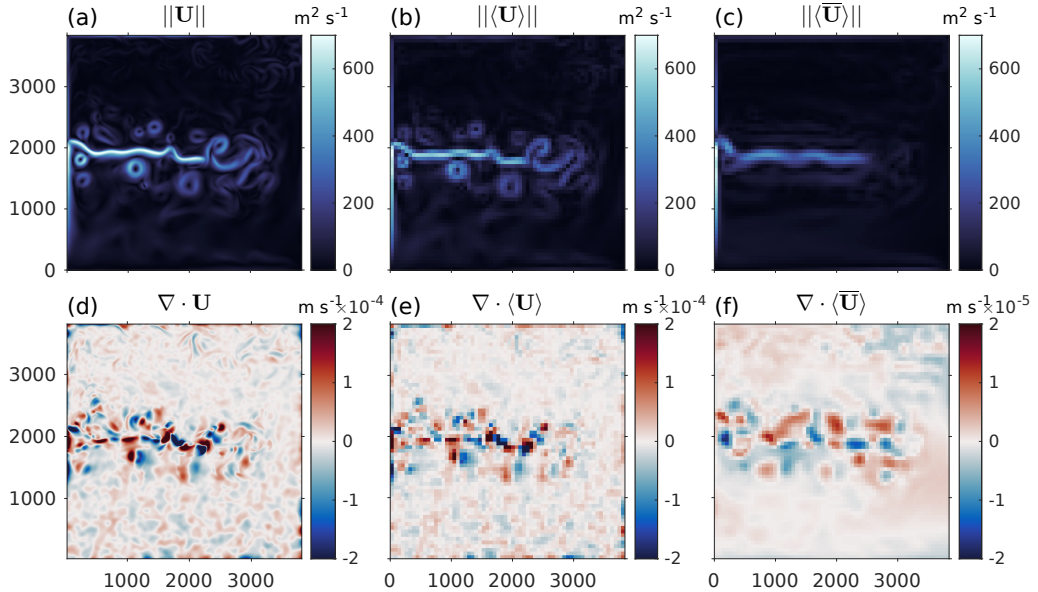


Figure 16: Norm of (a) the high-resolution mass flux, (b) the coarse-grained mass flux, and (c) the large-scale mass flux \bar{U}_L (coarse-grained and time filtered), at day 120 year 21 in the upper layer. (d)-(f) Divergences of the mass fluxes in (a)-(c), respectively. Note the color scale in (f) is ten times smaller than in (d) and (e).

740 weight $w = 1$, which was also tested in this study and did not affect our conclusions. Such
 741 correction that modifies the parameterized forcing has been widely applied to stochastic
 742 parameterizations in the operational ECMWF models (e.g. Leutbecher 2017).

743 We present the changes of the globally integrated tracer inventory, $\mathcal{M}_c = \int ch \, dx \, dy$,
 744 relative to its initial value for both the passive temperature and chemical tracers in figure
 745 17. The change in \mathcal{M}_c from the IDL_EEIV and CLOSURE experiments remain in the
 746 same range (< 0.1%) with that from the NO_EF and W_EF runs, confirming that the
 747 foregoing conservation modification works. Note that the total tracer inventory is not strictly
 748 conserved because of the relaxation surface boundary conditions, although such enforcement
 749 is straightforward to implement if desired (Lu *et al.* 2022).

REFERENCES

- 750 ADCROFT, A. ET AL. 2019 The GFDL Global Ocean and Sea Ice Model OM4.0: Model Description and
 751 Simulation Features. *J. Adv. Model. Earth Syst.* **11** (10), 3167–3211.
 752 AGARWAL, N., RYZHOV, E., KONDRAKHOV, D. & BERLOFF, P. 2021 Correlation-based flow decomposition and
 753 statistical analysis of the eddy forcing. *J. Fluid Mech.* **924**, A5.
 754 BACHMAN, S. 2019 The GM+E closure: A framework for coupling backscatter with the Gent and McWilliams
 755 parameterization. *Ocean Modell.* **136**, 85–106.
 756 BACHMAN, S., FOX-KEMPER, B. & BRYAN, F. 2015 A tracer-based inversion method for diagnosing eddy-
 757 induced diffusivity and advection. *Ocean Modell.* **86**, 1–14.
 758 BACHMAN, S., FOX-KEMPER, B. & PEARSON, B. 2017 A scale-aware subgrid model for quasi-geostrophic
 759 turbulence. *J. Geophys. Res. Oceans* **122** (2), 1529–1554.
 760 BACHMAN, SCOTT D., FOX-KEMPER, BAYLOR & BRYAN, FRANK O. 2020 A Diagnosis of Anisotropic Eddy
 761 Diffusion From a High-Resolution Global Ocean Model. *J. Adv. Model. Earth Syst.* **12** (2).
 762 BELKIN, I., CORNILLON, P. & SHERMAN, K. 2009 Fronts in Large Marine Ecosystems. *Prog. Oceanogr.*
 763 **81** (1-4), 223–236.
 764 BERLOFF, P. 2005 On dynamically consistent eddy fluxes. *Dyn. Atmos. Oceans* **38** (3), 123–146.

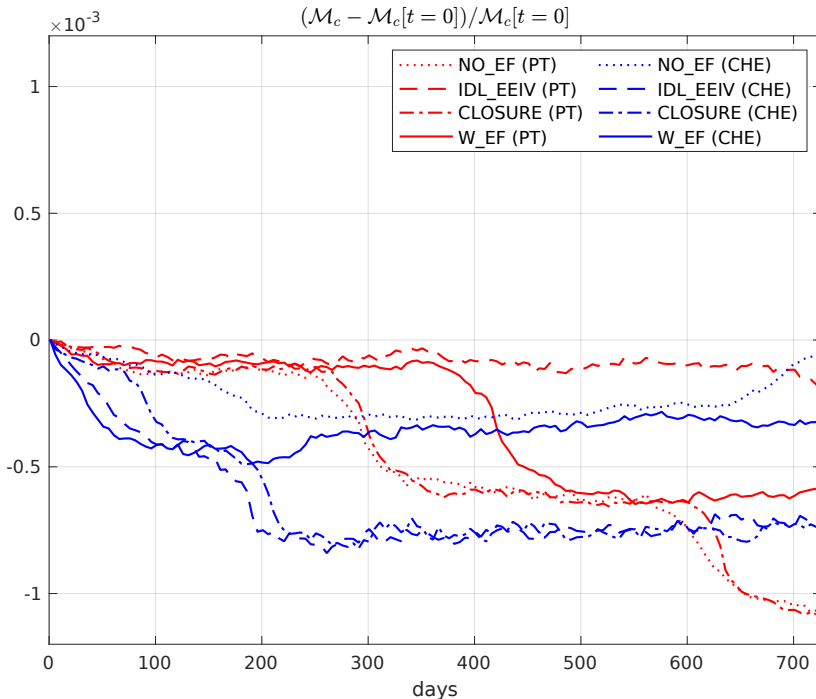


Figure 17: Evolution of the changes in the integrated tracer mass relative to the initial value from different experiments in the upper layer. Red is for the passive temperature tracer and blue is for the chemical tracer.

- 765 BERLOFF, PAVEL 2018 Dynamically consistent parameterization of mesoscale eddies. Part III: Deterministic
766 approach. *Ocean Modell.* **127**, 1–15.
767 BERLOFF, P., KAMENKOVICH, I. & PEDLOSKY, J. 2009 A model of multiple zonal jets in the oceans: Dynamical
768 and kinematical analysis. *J. Phys. Oceanogr.* **39** (11), 2711–2734.
769 BERLOFF, P., RYZHOV, E. & SHEVCHENKO, I. 2021 On dynamically unresolved oceanic mesoscale motions.
770 *J. Fluid Mech.* **920**, A41.
771 COOPER, F. & ZANNA, L. 2015 Optimisation of an idealised ocean model, stochastic parameterisation of
772 sub-grid eddies. *Ocean Modell.* **88**, 38–53.
773 D’ASARO, E., LEE, C., RAINVILLE, L., HARCOURT, R. & THOMAS, L. 2011 Enhanced Turbulence and Energy
774 Dissipation at Ocean Fronts. *Science* **332** (6027), 318–322.
775 ENGLAND, M. H., GARÇON, V. & MINSTER, J. 1994 Chlorofluorocarbon uptake in a world ocean model: 1.
776 Sensitivity to the surface gas forcing. *J. Geophys. Res. Oceans* **99** (C12), 25215–25233.
777 FERRARI, R. 2011 A Frontal Challenge for Climate Models. *Science* **332** (6027), 316–317.
778 GENT, P. & McWILLIAMS, J. 1990 Isopycnal Mixing in Ocean Circulation Models. *J. Phys. Oceanogr.* **20** (1),
779 150–155.
780 GENT, P., WILLEBRAND, J., McDougall, T. & McWILLIAMS, J. 1995 Parameterizing Eddy-Induced Tracer
781 Transports in Ocean Circulation Models. *J. Phys. Oceanogr.* **25** (4), 463–474.
782 GROOMES, I. 2016 A Gaussian-product stochastic Gent–McWilliams parameterization. *Ocean Modell.* **106**,
783 27–43.
784 GROOMES, I. & KLEIBER, W. 2019 Diagnosing, modeling, and testing a multiplicative stochastic Gent–
785 McWilliams parameterization. *Ocean Modell.* **133**, 1–10.
786 GUILLAUMIN, A. & ZANNA, L. 2021 Stochastic-Deep Learning Parameterization of Ocean Momentum
787 Forcing. *J. Adv. Model. Earth Syst.* **13** (9), e2021MS002534.
788 HAIGH, M. & BERLOFF, P. 2021 On co-existing diffusive and anti-diffusive tracer transport by oceanic
789 mesoscale eddies. *Ocean Modell.* **168**, 101909.
790 HAIGH, M. & BERLOFF, P. 2022 On the stability of tracer simulations with opposite-signed diffusivities. *J.*
791 *of Fluid Mech.* **937**, R3.

- 792 HAIGH, M., SUN, L., McWILLIAMS, J. & BERLOFF, P. 2021a On eddy transport in the ocean. Part I: The
793 diffusion tensor. *Ocean Modell.* **164**, 101831.
- 794 HAIGH, M., SUN, L., McWILLIAMS, J. & BERLOFF, P. 2021b On eddy transport in the ocean. Part II: The
795 advection tensor. *Ocean Modell.* **165**, 101845.
- 796 HAIGH, M., SUN, L., SHEVCHENKO, I. & BERLOFF, P. 2020 Tracer-based estimates of eddy-induced
797 diffusivities. *Deep Sea Res. I: Oceanogr. Res. Pap.* **160**, 103264.
- 798 HANEY, R. 1971 Surface Thermal Boundary Condition for Ocean Circulation Models. *J. Phys. Oceanogr.*
799 **1** (4), 241–248.
- 800 HEWITT, H. ET AL. 2020 Resolving and Parameterising the Ocean Mesoscale in Earth System Models. *Curr
801 Clim Change Rep* **6** (4), 137–152.
- 802 HOSKINS, B. 1982 The Mathematical Theory of Frontogenesis. *Annu. Rev. Fluid Mech.* **14** (1), 131–151.
- 803 KAMENKOVICH, I., BERLOFF, P., HAIGH, M., SUN, L. & LU, Y. 2021 Complexity of Mesoscale Eddy Diffusivity
804 in the Ocean. *Geophys. Res. Lett.* **48** (5).
- 805 KAMENKOVICH, I., BERLOFF, P. & IRINA, R. 2019 Anisotropic and inhomogeneous eddy-induced transport
806 in flows with jets. In *Zonal jets: Phenomenology, genesis, and physics*, pp. 437–449. Cambridge
807 University Press.
- 808 KAMENKOVICH, I. & GARRAFO, Z. 2022 Importance of Mesoscale Currents in Amoc Pathways and
809 Timescales. *J. Phys. Oceanogr.* **52** (8), 1613–1628.
- 810 KAMENKOVICH, I., GARRAFO, Z., PENNEL, R. & FINE, R. 2017 Importance of mesoscale eddies and mean
811 circulation in ventilation of the Southern Ocean. *J. Geophys. Res. Oceans* **122** (4), 2724–2741.
- 812 KIRTMAN, B. ET AL. 2012 Impact of ocean model resolution on CCSM climate simulations. *Clim. Dyn.*
813 **39** (6), 1303–1328.
- 814 LEUTBECHER, M. ET AL. 2017 Stochastic representations of model uncertainties at ECMWF: state of the art
815 and future vision. *Quart. J. Roy. Meteor. Soc.* **143** (707), 2315–2339.
- 816 LI, Q. & LEE, S. 2017 A Mechanism of Mixed Layer Formation in the Indo–Western Pacific Southern Ocean:
817 Preconditioning by an Eddy-Driven Jet-Scale Overturning Circulation. *J. Phys. Oceanogr* **47** (11),
818 2755–2772.
- 819 LI, Q., LEE, S. & GRIESEL, A. 2016 Eddy Fluxes and Jet-Scale Overturning Circulations in the Indo–Western
820 Pacific Southern Ocean. *J. Phys. Oceanogr* **46** (10), 2943–2959.
- 821 LOHMANN, R. & BELKIN, I. 2014 Organic pollutants and ocean fronts across the Atlantic Ocean: A review.
822 *Progress in Oceanography* **128**, 172–184.
- 823 LU, Y., KAMENKOVICH, I. & BERLOFF, P. 2022 Properties of the Lateral Mesoscale Eddy-Induced Transport
824 in a High-Resolution Ocean Model: Beyond the Flux–Gradient Relation. *J. Phys. Oceanogr.* **52** (12),
825 3273–3295.
- 826 MADDISON, J.R., MARSHALL, D.P. & SHIPTON, J. 2015 On the dynamical influence of ocean eddy potential
827 vorticity fluxes. *Ocean Modell.* **92**, 169–182.
- 828 MANA, P. & ZANNA, L. 2014 Toward a stochastic parameterization of ocean mesoscale eddies. *Ocean Modell.*
829 **79**, 1–20.
- 830 MCWILLIAMS, J. 2016 Submesoscale currents in the ocean. *Proc. R. Soc. A* **472** (2189), 20160117.
- 831 MCWILLIAMS, J. 2021 Oceanic Frontogenesis. *Annu. Rev. Fluid Mech.* **13** (1), 227–253.
- 832 MEIJERS, A 2014 The Southern Ocean in the Coupled Model Intercomparison Project phase 5. *Phil. Trans.
R. Soc. A.* **372** (2019), 20130296.
- 833 MINOBE, S., KUWANO-YOSHIDA, A., KOMORI, N., XIE, S.-P. & SMALL, J. 2008 Influence of the Gulf Stream
834 on the troposphere. *Nature* **452** (7184), 206–209.
- 835 MUDRICK, S. 1974 A Numerical Study of Frontogenesis. *J. Atmos. Sci.* **31** (4), 869–892.
- 836 NAKAMURA, N. 1996 Two-Dimensional Mixing, Edge Formation, and Permeability Diagnosed in an Area
837 Coordinate. *J. Atmos. Sci.* **53** (11), 1524–1537.
- 838 PARFITT, R., CZAJA, A., MINOBE, S. & KUWANO-YOSHIDA, A. 2016 The atmospheric frontal response to SST
839 perturbations in the Gulf Stream region. *Geophys. Res. Lett.* **43** (5), 2299–2306.
- 840 PARTEE, S., ELLIS, M., RIGAZZI, A., SHAO, A., BACHMAN, S., MARQUES, G. & ROBBINS, B. 2022 Using
841 Machine Learning at scale in numerical simulations with SmartSim: An application to ocean climate
842 modeling. *J. Comput. Sci.* **62**, 101707.
- 843 PATCHING, S. 2022 On divergence- and gradient-preserving coarse-graining for finite volume primitive
844 equation ocean models. *Ocean Modell.* **170**, 101941.
- 845 PEDLOSKY, J. 1987 *Geophysical Fluid Dynamics*. Springer New York.
- 846 REDI, M. 1982 Oceanic Isopycnal Mixing by Coordinate Rotation. *J. Phys. Oceanogr.* **12** (10), 1154–1158.

- 848 ROSS, A., LI, Z., PEREZHOGIN, P., FERNANDEZ-GRANDA, C. & ZANNA, L. 2023 Benchmarking of Machine
 849 Learning Ocean Subgrid Parameterizations in an Idealized Model. *J. Adv. Model. Earth Syst.* **15** (1),
 850 e2022MS003258.
- 851 RYPINA, I., JAYNE, S., YOSHIDA, S., MACDONALD, A. M., DOUGLASS, E. & BUSSERLER, K. 2013 Short-
 852 term dispersal of Fukushima-derived radionuclides off Japan: modeling efforts and model-data
 853 intercomparison. *Biogeosciences* **10** (7), 4973–4990.
- 854 RYPINA, I., PRATT, L. & LOZIER, S. 2011 Near-Surface Transport Pathways in the North Atlantic Ocean:
 855 Looking for Throughput from the Subtropical to the Subpolar Gyre. *J. Phys. Oceanogr.* **41** (5),
 856 911–925.
- 857 RYZHOV, E. & BERLOFF, P. 2022 On transport tensor of dynamically unresolved oceanic mesoscale eddies.
 858 *J. Fluid Mech.* **939**, A7.
- 859 SEO, H. ET AL. 2023 Ocean Mesoscale and Frontal-Scale Ocean–Atmosphere Interactions and Influence on
 860 Large-Scale Climate: A Review. *J. Climate* **36** (7), 1981–2013.
- 861 SHEVCHENKO, I. & BERLOFF, P. 2015 Multi-layer quasi-geostrophic ocean dynamics in Eddy-resolving
 862 regimes. *Ocean Modell.* **94**, 1–14.
- 863 SIQUEIRA, L. & KIRTMAN, B. 2016 Atlantic near-term climate variability and the role of a resolved Gulf
 864 Stream. *Geophys. Res. Lett.* **43** (8), 3964–3972.
- 865 SMAGORINSKY, J. 1963 General circulation experiments with the primitive equations: I. The basic experiment.
 866 *Mon. Weather Rev.* **91** (3), 99–164.
- 867 SMALL, J., DESZOEKE, S.P., XIE, S.P., O'NEILL, L., SEO, H., SONG, Q., CORNILLON, P., SPALL, M. & MINOBE,
 868 S. 2008 Air-sea interaction over ocean fronts and eddies. *Dyn. Atmos. Oceans* **45** (3-4), 274–319.
- 869 SMALL, J., TOMAS, R. & BRYAN, F. 2014 Storm track response to ocean fronts in a global high-resolution
 870 climate model. *Clim. Dyn.* **43** (3), 805–828.
- 871 SUN, L., HAIGH, M., SHEVCHENKO, I., BERLOFF, P. & KAMENKOVICH, I. 2021 On non-uniqueness of the
 872 mesoscale eddy diffusivity. *J. Fluid Mech.* **920**, A32.
- 873 TRIAS, F., DABBAGH, F., GOROBETS, A. & OLIET, C. 2020 On a Proper Tensor-Diffusivity Model for Large-
 874 Eddy Simulation of Buoyancy-Driven Turbulence. *Flow Turbul. Combust.* **105** (2), 393–414.
- 875 UCHIDA, T., DEREMBLE, B. & POPINET, S. 2022 Deterministic Model of the Eddy Dynamics for a Midlatitude
 876 Ocean Model. *J. Phys. Oceanogr.* **52** (6), 1133–1154.
- 877 VALLIS, G. K. 2017 *Atmospheric and Oceanic Fluid Dynamics*. Cambridge University Press.
- 878 WATERMAN, S., HOGG, N. & JAYNE, S. 2011 Eddy–Mean Flow Interaction in the Kuroshio Extension Region.
 879 *J. Phys. Oceanogr.* **41** (6), 1182–1208.
- 880 WATERMAN, S. & JAYNE, S. 2011 Eddy-Mean Flow Interactions in the Along-Stream Development of a
 881 Western Boundary Current Jet: An Idealized Model Study. *J. Phys. Oceanogr.* **41** (4), 682–707.
- 882 YANKOVSKY, E., ZANNA, L. & SMITH, S. 2022 Influences of Mesoscale Ocean Eddies on Flow
 883 Vertical Structure in a Resolution-Based Model Hierarchy. *J. Adv. Model. Earth Syst.* **14** (11),
 884 e2022MS003203.
- 885 ZANNA, L. & BOLTON, T. 2020 Data-Driven Equation Discovery of Ocean Mesoscale Closures. *Geophys.
 886 Res. Lett.* **47** (17), e2020GL088376.
- 887 ZANNA, L., MANA, P., ANSTEY, J., DAVID, T. & BOLTON, T. 2017 Scale-aware deterministic and stochastic
 888 parametrizations of eddy-mean flow interaction. *Ocean Modell.* **111**, 66–80.
- 889 ZHANG, C., PEREZHOGIN, P., GULTEKIN, C., ADCROFT, A., FERNANDEZ-GRANDA, C. & ZANNA, L. 2023
 890 Implementation and Evaluation of a Machine Learned Mesoscale Eddy Parameterization Into a
 891 Numerical Ocean Circulation Model. *J. Adv. Model. Earth Syst.* **15** (10), e2023MS003697.
- 892 ZHANG, W. & WOLFE, C. 2022 On the Vertical Structure of Oceanic Mesoscale Tracer Diffusivities. *J. Adv.
 893 Model. Earth Syst.* **14** (6).